



# The optimal configuration of negative stiffness inerter-based base isolators in multi-storey buildings

Sudip Chowdhury<sup>a,\*</sup>, Arnab Banerjee<sup>a</sup>, Sondipon Adhikari<sup>b</sup>

<sup>a</sup> Civil Engineering Department, Indian Institute of Technology Delhi, India

<sup>b</sup> James Watt School of Engineering, The University of Glasgow, Glasgow, Scotland, UK

## ARTICLE INFO

### Keywords:

Negative stiffness inerter-based base isolators  
Conventional base isolators  
Five and ten-storey buildings  
Dynamic response reduction capacities  
 $H_2$  optimization method

## ABSTRACT

The negative stiffness inerter-based base isolators (NSIBI) are introduced in this paper. The negative stiffness device and inerters are installed inside the core of the conventional base isolators (CBI) to enhance their dynamic response reduction capacity. The novel isolators have been installed at the multi-storey building's base to mitigate their dynamic responses during vibration.  $H_2$  optimization method applies to derive the exact closed-form expression for negative stiffness inerter-based base isolators' optimal design parameters, such as frequency and viscous damping ratio for multi-storey buildings. Applying these  $H_2$  optimized design parameters, the optimum NSIBI for dynamic response mitigation of multi-storey buildings have been achieved. The dynamic responses of the NSIBI-controlled multi-storey buildings are compared with the dynamic responses of multi-storey buildings isolated by optimum CBI to determine the exact superior dynamic response reduction capacity of optimum NSIBI. The dynamic responses of isolated structures in the frequency domain are evaluated by forming the transfer function. Therefore, for five-storey buildings, the dynamic response reduction capacity of NSIBI is significantly 51.93% and 81.24% superior to the dynamic response reduction capacity of CBI subjected to harmonic and random-white excitations. In contrast, for ten-storey buildings, the optimum NSIBI has 77.73% and 94.02% more dynamic response reduction capacity than the optimum CBI subjected to harmonic and random-white excitations. In addition, using the Newmark beta method, a numerical study further conducts to verify the accuracy of the  $H_2$  optimized design parameters by obtaining the time history results for isolated structures subjected to near-field pulse-type earthquake base excitations. Accordingly, the optimum NSIBI have 57.591% and 55.398% more displacement and acceleration capacity than the optimum CBI for five-storey buildings. Besides, for ten-storey buildings, the displacement and acceleration capacities of optimum NSIBI are significantly around 56.42% and 55.80%, superior to the optimum CBI. Thus, the vibration reduction capacity of optimum CBI is significantly decreasing while the storey level of the multi-storey buildings increases, whereas NSIBI is still efficient in reducing the dynamic responses effectively. The paper's outcomes are mathematically accurate and applicable to practical implementation.

## 1. Introduction

To protect structures and individuals from natural disasters like earthquakes and heavy storms, the base isolation devices are preferable to all other passive vibration control devices [1–3]. In order to mitigate the dynamic responses during vibration, the base isolation devices are installed in an assortment of structures, such as aircraft landing gear [4,5], buildings [6], bridges [7], liquid storage tanks [8], and vehicle suspension [9]. Among all dynamic systems, precisely from civil engineering structures, the dynamic responses of the buildings and bridges are controlled by the base isolation systems. These isolation devices are installed between the dynamic systems' substructure

and superstructure [10–13]. The dynamic responses of the linear isolators [14] are determined by considering the entire isolator as a mass–spring–dash pot and mathematically derive [15], through transfer function [16], analytically derive straightforward solutions [17]. The viscous damping ratio considers for linear isolators. However, the nonlinear isolators are mathematically formulated by replacing the viscous damping [18] ratio through hysteresis [19], and non-viscous damping [18]. New Zealand bearing [20], lead rubber bearing [21], resilient friction base isolator [22], friction-pendulum system [23,24], and pure friction system [25] are the nonlinear base isolation devices [26], applicable for the structures for vibration reduction. Particularly for building structures, the isolators [27–32] are installed at the base of

\* Corresponding author.

E-mail address: [sudip.chowdhury@civil.iitd.ac.in](mailto:sudip.chowdhury@civil.iitd.ac.in) (S. Chowdhury).

<https://doi.org/10.1016/j.istruc.2023.02.095>

Received 5 September 2022; Received in revised form 17 February 2023; Accepted 20 February 2023

Available online 28 February 2023

2352-0124/© 2023 Institution of Structural Engineers. Published by Elsevier Ltd. All rights reserved.

single-storey and multi-storey buildings and the isolated structures are mathematically formulated by considering SDOF and MDOF systems. For isolated MDOF structures [33], the modal superposition method is most preferably applicable to analyse the dynamic responses.

In addition, to achieve robustness in vibration reduction from the isolators, the optimal design parameters for the isolators need to be determined [34–36]. There are different types of analytical and numerical optimization methods available. Among all optimization methods in the domain of analytical optimization schemes,  $H_2$  and  $H_\infty$  methods are the most prominent ones [37–40]. The mathematical formulations in terms of closed-form expressions for optimal design parameters of the isolators are obtained [41]. The optimal closed-form expressions for the stochastic  $H_2$  optimization method emerge from the standard deviation of the primary structure’s responses to random vibration of the isolated structures [42,43]. In contrast, applying the  $H_\infty$  optimization method, the exact closed-form expressions for optimal design parameters are obtained to minimize the dynamic response of the primary structure [44] as using this method, the equations of motion of the complete MDOF system can be decoupled into the equation of motion of the individual SDOF systems for each degree of freedom. From the perspective of the working principle of traditional base isolators, the base isolator provides larger displacement at the isolation layer, which is undesirable as it can damage the isolation floor for higher amplitude earthquakes [45]. These over-increased time periods of the isolated structure can also reduce the isolator’s adaptability when the ground motion load pattern changes from near-fault to far-field [46]. The traditional base isolators become less efficient for high-rise buildings in terms of vibration reduction. These scenarios need to be reduced, which motivates researchers to find an alternative way to enhance its adaptability and performance [47].

Therefore, considering the advantages and disadvantages of the traditional isolators, to overcome the above-mentioned disadvantages of the traditional isolators, the vibration reduction capacity of the traditional isolators in recent days increased using effective mass amplification devices, named inerters [48–50] and inertial amplifiers [51–55]. In addition, the applications of negative stiffness [56,57], negative mass [58–60], negative Young modulus [61–63], and other devices [64–66] to traditional isolators for increasing their vibration reduction capacity plus minimizing the structures’ dynamic responses. Magnetic negative stiffness dampers [67], pseudo-negative stiffness [68], high-static-low-dynamic stiffness [69,70], and Euler buckled beams [71,72], negative-stiffness inclusions [73] are used as negative stiffness elements in the traditional base isolators to increase their vibration reduction capacity. However, a combination of negative stiffness devices and inerters does not apply to the traditional base isolators to overcome the above-mentioned disadvantages of the traditional isolators, plus the rigorous explicit analytical closed-form mathematical formulations for the optimal design parameters of the novel isolator have not been studied and presented in the existing state-of-the-art. Accordingly, a research scope identifies.

The negative stiffness inerter-based base isolators (NSIBI) are introduced in this paper to address the above-stated research scope. The novel isolators are installed at the base of the multi-storey buildings to reduce the dynamic responses of the isolated structures during vibratory circumstances.  $H_2$  optimization methods are applied to derive the exact mathematical closed-form formulations for optimal design parameters such as the natural frequency and viscous damping ratio of NSIBI. Initially, to verify the accuracy of the  $H_2$  optimized closed-form solutions for the isolators, the dynamic responses, and the corresponding dynamic response reduction capacity of multi-storey buildings isolated by traditional or conventional base isolators (CBI) and negative stiffness inerter-based base isolators (NSIBI) are derived analytically through transfer function formations subjected to harmonic and random-white noise base excitations. Later, a numerical study, considering the Newmark-beta method, has been performed to verify the accuracy of the  $H_2$  optimized closed-form solutions for the isolators

with the time-domain responses. The near-field earthquake records are induced in the design as seismic base excitations to conduct the time history analysis and determine time domain responses. Furthermore, the dynamic response reduction capacity of the optimum NSIBI has been compared w.r.t the optimum CBI.

## 2. Methodology

### 2.1. Structural model

The schematic diagram of a multi-storey building isolated by negative stiffness inerter-base vibration isolator has been shown in Fig. 1. The NSIBI systems are installed at the base of the multi-storey buildings subjected to base excitations.  $m_b$ ,  $k_b$ , and  $c_b$  refer to the mass, stiffness, and damping of the NSIBI.  $m_d$  refers to the mass of the inerter.  $k_d$  refers to the stiffness of the negative stiffness device. ‘N’ refers to the number of floors for the superstructure.  $m_N$ ,  $k_N$ , and  $c_N$  define the mass, stiffness, and damping of the top floor.  $m_1$ ,  $k_1$ , and  $c_1$  refer to the mass, stiffness, and damping of the first floor.  $x_g$ ,  $u_b$ ,  $u_1$ , and  $u_N$  refer to the displacement of base excitation, isolator, first floor, and the top floor during vibration.

### 2.2. Equations of motion

Newton’s second law has been applied to derive the equations of motion for isolated multi-storey buildings. The governing equations of motion of multi-storey buildings isolated by negative stiffness inerter-based isolation systems have been derived as

$$[\mathbf{M}_s]\{\ddot{\mathbf{x}}_s\} + [\mathbf{C}_s]\{\dot{\mathbf{x}}_s\} + [\mathbf{K}_s]\{\mathbf{x}_s\} = -[\mathbf{M}_s]\{\mathbf{r}\}(\ddot{x}_g + \ddot{x}_b) \tag{1}$$

$$m_b\ddot{x}_b + m_d\ddot{x}_b + c_b\dot{x}_b + (k_b - k_d)x_b - k_1x_1 - c_1\dot{x}_1 = -m_b\ddot{x}_g$$

where,  $x_b = u_b - x_g$  refers to the relative displacement of isolator.  $x_N = u_N - u_b$ ,  $x_{N-1} = u_{N-1} - u_b$ , and  $x_1 = u_1 - u_b$  refer to the relative displacement of each floor.  $[\mathbf{M}_s]$ ,  $[\mathbf{C}_s]$ , and  $[\mathbf{K}_s]$  refer to the mass, viscous damping, and stiffness matrix of the superstructure.  $\{\mathbf{x}_s\} = \{x_1, x_2, x_3, \dots, x_N\}$ ,  $\{\dot{\mathbf{x}}_s\}$ , and  $\{\ddot{\mathbf{x}}_s\}$  refer to the unknown relative displacement, acceleration, and velocity vectors for the superstructure.  $\{\mathbf{r}\} = \{1, 1, 1, \dots, 1\}$  refers to the influence coefficients vector. Five-storey building lies in the class of the acceleration control range. Hence, first, a five-storey building has been considered to derive the dynamic responses of the isolated multi-storey buildings analytically.

$$m_b\ddot{x}_b + m_d\ddot{x}_b + c_b\dot{x}_b + (k_b - k_d)x_b - k_1x_1 - c_1\dot{x}_1 = -m_b\ddot{x}_g$$

$$m_1\ddot{x}_1 + (c_1 + c_2)\dot{x}_1 - c_2\dot{x}_2 + (k_1 + k_2)x_1 - k_2x_2 + m_1\ddot{x}_b = -m_1\ddot{x}_g$$

$$m_2\ddot{x}_2 - c_2\dot{x}_1 + (c_2 + c_3)\dot{x}_2 - c_3\dot{x}_3 - k_2x_1 + (k_2 + k_3)x_2 - k_3x_3 + m_2\ddot{x}_b = -m_2\ddot{x}_g$$

$$m_3\ddot{x}_3 - c_3\dot{x}_2 + (c_3 + c_4)\dot{x}_3 - c_4\dot{x}_4 - k_3x_2 + (k_3 + k_4)x_3 - k_4x_4 + m_3\ddot{x}_b = -m_3\ddot{x}_g$$

$$m_4\ddot{x}_4 - c_4\dot{x}_3 + (c_4 + c_5)\dot{x}_4 - c_5\dot{x}_5 - k_4x_3 + (k_4 + k_5)x_4 - k_5x_5 + m_4\ddot{x}_b = -m_4\ddot{x}_g$$

$$m_5\ddot{x}_5 - c_5\dot{x}_4 + c_5\dot{x}_5 - k_5x_4 + k_5x_5 + m_5\ddot{x}_b = -m_5\ddot{x}_g$$

where  $m_1$ ,  $m_2$ ,  $m_3$ ,  $m_4$ ,  $m_5$  refers to the mass of each floor and is considered as same, i.e.,  $m_1 = m_2 = m_3 = m_4 = m_5 = m_s$ .  $k_1$ ,  $k_2$ ,  $k_3$ ,  $k_4$ ,  $k_5$  refers to the stiffness of each floor and is considered as same, i.e.,  $k_1 = k_2 = k_3 = k_4 = k_5 = k_s$ .  $c_1$ ,  $c_2$ ,  $c_3$ ,  $c_4$ ,  $c_5$  refers to the damping of each floor and is considered as same, i.e.,  $c_1 = c_2 = c_3 = c_4 = c_5 = c_s$ . The steady-state solutions for the dynamic responses of isolated structures subjected to harmonic base excitations are derived as  $x_1 = X_1e^{i\omega t}$ ,  $x_2 = X_2e^{i\omega t}$ ,  $x_3 = X_3e^{i\omega t}$ ,  $x_4 = X_4e^{i\omega t}$ ,  $x_5 = X_5e^{i\omega t}$ ,  $x_b = X_be^{i\omega t}$ , and  $\ddot{x}_g = A_g e^{i\omega t}$ . Therefore, a transfer function has been formed to derive the dynamic responses of the multi-storey buildings

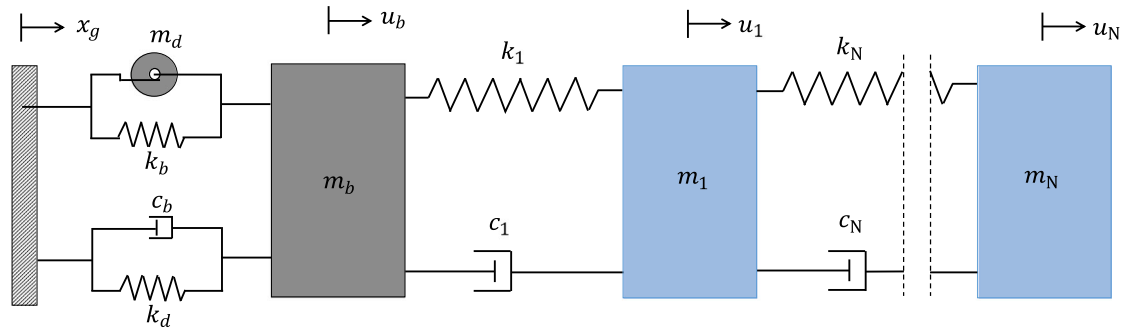


Fig. 1. The schematic diagram of multi-storey building isolated by negative stiffness inerter-based base isolator subjected to base excitations.

after substituting the steady state solutions into Eq. (2) and expressed as

$$\begin{bmatrix} B_1 & B_2 & 0 & 0 & 0 & q^2 \\ B_2 & B_1 & B_2 & 0 & 0 & q^2 \\ 0 & B_2 & B_1 & B_2 & 0 & q^2 \\ 0 & 0 & B_2 & B_1 & B_2 & q^2 \\ 0 & 0 & 0 & B_2 & B_3 & q^2 \\ B_2 & 0 & 0 & 0 & 0 & B_4 \end{bmatrix} \begin{Bmatrix} X_1 \\ X_2 \\ X_3 \\ X_4 \\ X_5 \\ X_b \end{Bmatrix} = - \begin{bmatrix} 1 \\ 1 \\ 1 \\ 1 \\ 1 \\ \mu_b \end{bmatrix} A_g \quad (3)$$

$$q = i\omega, B_1 = 4 \zeta_s q \omega_s + q^2 + 2 \omega_s^2, B_2 = -2 \zeta_s q \omega_s - \omega_s^2, B_3 = 2 \zeta_s q \omega_s + q^2 + \omega_s^2$$

$$\text{and } B_4 = (\mu_b + \mu_d) q^2 + 2 \zeta_b q \omega_b (\mu_b + \mu_d) + \omega_b^2 (\mu_b + \mu_d) - \beta \omega_b^2 (\mu_b + \mu_d) \quad (4)$$

where  $\mu_b = m_b/m_s$  refers to the base mass ratio.  $\mu_d = m_d/m_s$  refers to the inerter mass ratio.  $\omega_b = \sqrt{k_b/(m_b + m_d)}$  refers to the natural frequency of the isolator.  $\eta_b = \omega_b/\omega_s$  refers to the frequency ratio of the isolator.  $\omega_s = \sqrt{k_s/m_s}$  refers to the natural frequency of the each floor.  $\zeta_b = \frac{c_b}{2(m_b+m_d)\omega_b}$  refers to the viscous damping ratio of the isolator.  $\beta = k_d/k_b$  refers to the stiffness ratio of NSIBI.  $\zeta_s = \frac{c_s}{2m_s\omega_s}$  defines the viscous damping ratio of each floor. To perform the  $H_2$  optimization method for deriving the closed-form expressions for optimal design parameters of NSIBI analytically, the viscous damping ratio of each floor of the superstructure has been considered as  $\zeta_s = 0$ . Therefore, the dynamic response of the top floor of the five-storey building has been derived as

$$H_5(q) = \frac{X_5}{A_g} = \frac{\begin{pmatrix} (\mu_b + \mu_d)(\beta - 1)\omega_b^2 \\ -2q\zeta_b(\mu_b + \mu_d)\omega_b - q^2\mu_d \end{pmatrix}}{(q^2 + \omega_s^2)(q^4 + 5q^2\omega_s^2 + 5\omega_s^4)(q^2 + 3\omega_s^2)} \Delta \quad (5)$$

The Eqs. (5) and (A.2) apply further to derive mathematical closed-form formulations for optimal design parameters of NSIBI using  $H_2$  optimization method. The dynamic response of NSIBI and the closed-form expression for  $\Delta$  has been listed in Appendix A. The total effective mass of the negative stiffness inerter-based isolators has been derived as  $m_e = m_b + m_d$ . The effective mass ratio has been derived as

$$\mu_e = \frac{m_b + m_d}{m_s} = \mu_b + \mu_d \quad (6)$$

The total effective stiffness of the negative stiffness inerter-based isolator has been derived as

$$k_e = k_b - k_d = k_b(1 - \beta) \quad (7)$$

where  $\beta = k_d/k_b$  refers to the stiffness ratio of NSIBI. The effective stiffness of NSIBI has been divided by the stiffness of each floor of the main structure, i.e.,  $\nu = k_e/k_s$ .  $\nu$  has also been named as an ‘‘isolator

effective to each floor of main structure stiffness ratio’’. Accordingly,  $\nu$  has been derived as

$$\nu = \frac{k_e}{k_s} = (\mu_b + \mu_d) \eta_b^2 (1 - \beta) \quad (8)$$

Applying Eq. (8), the variations of isolator effective to each floor of main structure stiffness ratio versus stiffness ratio for different values of inerter mass ratio have been shown in Fig. 2(a).  $\mu_b = 0.8$  considers for this graph.  $\nu$  decreases as the stiffness ratio increases while  $\nu$  increases as the inerter mass ratio increases. In addition, the variations of isolator effective to each floor of the main structure stiffness ratio versus stiffness ratio for different values of base mass ratio have been shown in Fig. 2(b).  $\mu_d = 0.3$  considers for this graph.  $\nu$  decreases as the stiffness ratio increases while  $\nu$  increases as the base mass ratio increases. Only for Fig. 2,  $\eta_b = 0.4$  has been considered to find out the effectiveness of  $\beta$  on the total effective stiffness of the negative stiffness inerter-based isolator. The higher values of  $\beta$  provide lower stiffness to the system, which indicates additional flexibility to the base, resulting in more dynamic response reduction capacity. From Fig. 2,  $\beta = 0.1$  has been selected for the study to investigate the vibration reduction performance of NSIBI for multi-storey buildings at its lower stiffness ratio region. The effective stiffness ratio has been derived as

$$\kappa_e = \frac{k_b - k_d}{k_b} = \frac{(\mu_b + \mu_d)(1 - \beta)}{\mu_b} \quad (9)$$

The graphical representations of effective mass ratio have been displayed in Fig. 3(a). The contour diagram of effective mass ratio as a function of inerter mass ratio and base mass ratio has been displayed as a graphical representation of Eq. (6). The effective mass ratio increases as the base mass ratio and inerter mass ratio increase. Additional effective mass decreases the natural frequency of the isolator, which increases the time period of the isolated structure during vibration. The graphical representations of the effective stiffness ratio have been displayed in Fig. 3(b). The contour diagram of the effective stiffness ratio as a function of inerter mass ratio and base mass ratio has been displayed as the graphical representation of Eq. (9). The effective stiffness ratio increases as the base mass ratio and inerter mass ratio increase. The additional effective stiffness provides sufficient load-bearing capacity to the isolated structures when the base becomes flexible due to the enhancement of the effective mass. Therefore, the negative stiffness inerter-based base isolator provides additional flexibility and simultaneously additional load-bearing capacity to the isolated structures, respectively.

### 3. $H_2$ optimization for NSIBI systems

The optimal design parameters for NSIBI have been derived analytically employing the  $H_2$  optimization method [34,40,74]. For applying

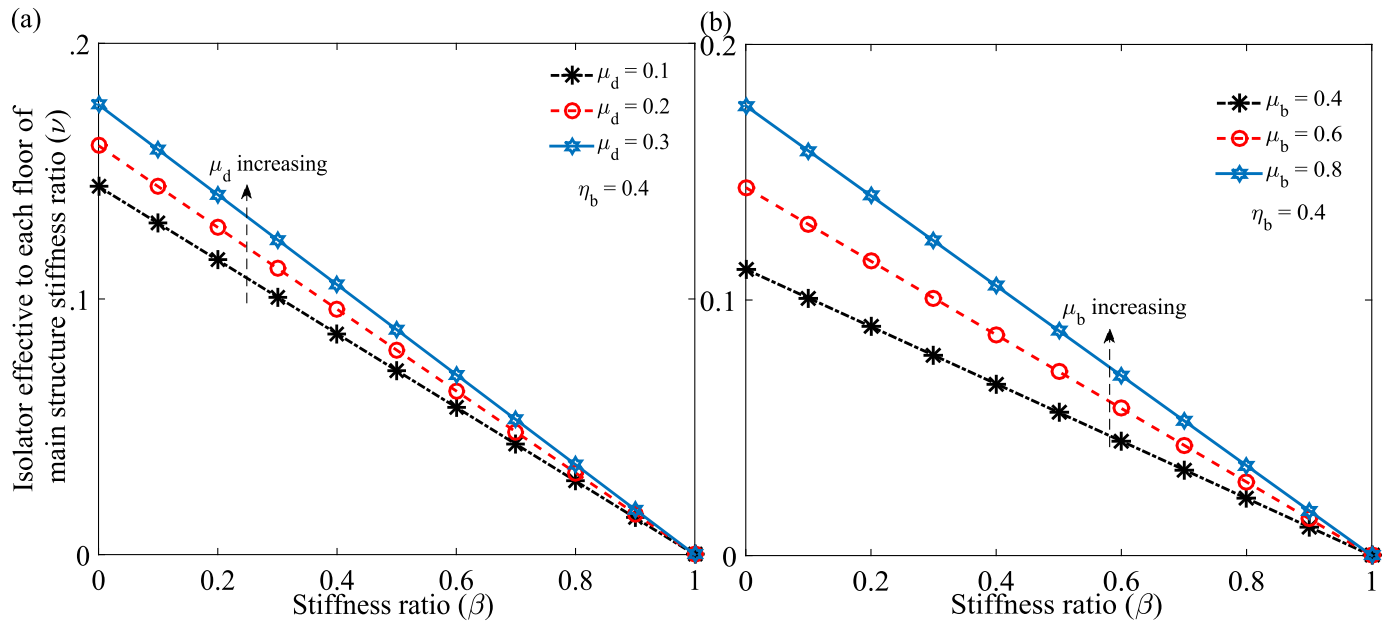


Fig. 2. The variations of isolator effective to each floor of main structure stiffness ratio versus stiffness ratio for different values of (a) inerter mass ratio and (b) base mass ratio.

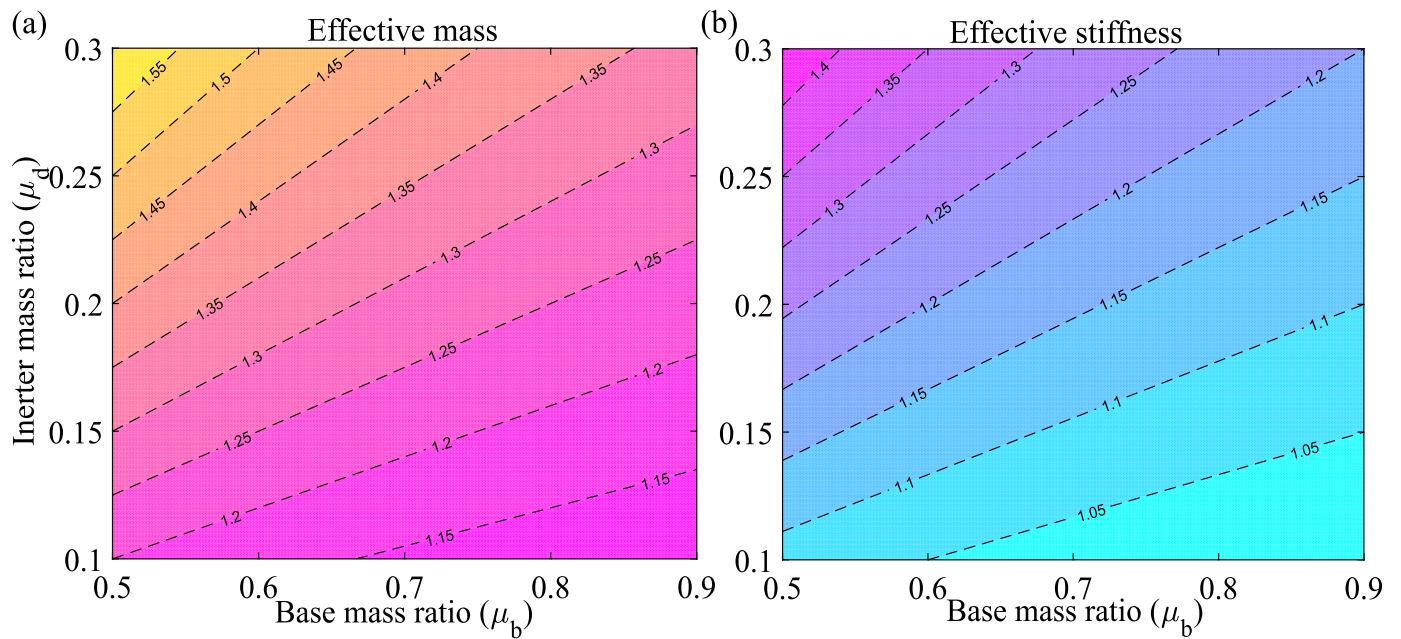


Fig. 3. The contour diagrams of (a) effective mass and (b) effective stiffness as a function of inerter mass ratio and base mass ratio.

this method, it has been considered that the isolated structures are subjected to random-white noise base excitations. The standard deviations (SD) of the dynamic responses of the superstructure have been minimized. Hence, Eq. (A.2) is a 12th order polynomial equation. The Eqs. (5) and (A.2) utilize to derive exact closed-form formulations for optimal design parameters of NSIBI using a mathematical formulation. Accordingly, the mathematical formulations to derive the exact closed-form expression for SD of the superstructures are presented in Appendix B. Therefore, applying Eqs. (B.1), (B.2), and (B.3) in Appendix B, the exact closed-form expression for SD of the dynamic

response of the top floor of the superstructure has been derived as

$$\sigma_{x_s}^2 = \frac{S_0 \pi \begin{pmatrix} 671 \beta^2 \mu_b^2 \omega_b^4 + 1342 \beta^2 \mu_b \mu_d \omega_b^4 + 671 \beta^2 \mu_d^2 \omega_b^4 \\ + 220 \zeta_b^2 \mu_b^2 \omega_b^2 \omega_s^2 + 440 \zeta_b^2 \mu_b \mu_d \omega_b^2 \omega_s^2 \\ - 1342 \beta \mu_b^2 \omega_b^4 - 2684 \beta \mu_b \mu_d \omega_b^4 + 110 \beta \mu_b \mu_d \omega_b^2 \omega_s^2 \\ - 1342 \beta \mu_d^2 \omega_b^4 + 110 \beta \mu_d^2 \omega_b^2 \omega_s^2 - 225 \beta \mu_b \omega_b^2 \omega_s^2 \\ - 225 \beta \mu_d \omega_b^2 \omega_s^2 + 671 \mu_b^2 \omega_b^4 + 1342 \mu_b \mu_d \omega_b^4 \\ - 110 \mu_b \mu_d \omega_b^2 \omega_s^2 + 671 \mu_d^2 \omega_b^4 - 110 \mu_d^2 \omega_b^2 \omega_s^2 \\ + 5 \mu_d^2 \omega_s^4 + 225 \mu_b \omega_b^2 \omega_s^2 + 225 \mu_d \omega_b^2 \omega_s^2 \\ + 220 \zeta_b^2 \mu_d^2 \omega_b^2 \omega_s^2 \end{pmatrix}}{2 \zeta_b \omega_b \omega_s^6 (\mu_b + \mu_d)} \quad (10)$$

Eq. (10) has been partially differentiated with respect to the viscous damping ratio  $\zeta_b$  and natural frequency  $\omega_b$  of NSIBI. The mathematical formulations for this partial differentiation [34] have been derived as

$$\frac{\partial \sigma_{x_s}^2}{\partial \zeta_b} = 0 \quad \text{and} \quad \frac{\partial \sigma_{x_s}^2}{\partial \omega_b} = 0 \tag{11}$$

First, Eq. (10) has been inserted into the first equation of Eq. (11). The closed-form expression for viscous damping ratio  $\zeta_b$  has been derived as

$$\zeta_b = \sqrt{\frac{671 \beta^2 \mu_b^2 \omega_b^4 + 1342 \beta^2 \mu_b \mu_d \omega_b^4 + 671 \beta^2 \mu_d^2 \omega_b^4 + 110 \beta \mu_b \mu_d \omega_b^2 \omega_s^2 - 1342 \beta \mu_d^2 \omega_b^4 + 110 \beta \mu_d^2 \omega_b^2 \omega_s^2 - 225 \beta \mu_b \omega_b^2 \omega_s^2 - 225 \beta \mu_d \omega_b^2 \omega_s^2 + 671 \mu_b^2 \omega_b^4 + 1342 \mu_b \mu_d \omega_b^4 - 110 \mu_b \mu_d \omega_b^2 \omega_s^2 + 671 \mu_d^2 \omega_b^4 - 110 \mu_d^2 \omega_b^2 \omega_s^2 + 5 \mu_d^2 \omega_s^4 + 225 \mu_b \omega_b^2 \omega_s^2 + 225 \mu_d \omega_b^2 \omega_s^2 - 1342 \beta \mu_b^2 \omega_b^4 - 2684 \beta \mu_b \mu_d \omega_b^4}{220 \mu_b^2 \omega_b^2 \omega_s^2 + 440 \mu_b \mu_d \omega_b^2 \omega_s^2 + 220 \mu_d^2 \omega_b^2 \omega_s^2}} \tag{12}$$

Eq. (12) has been inserted into Eq. (10). Hence, the modified SD has been listed in Appendix B, and the equation number is Eq. (B.4). Eq. (B.4) has been inserted into the second equation of Eq. (11). Therefore, the closed-form expression for the optimal frequency of the NSIBI has been derived as

$$(\omega_b)_{opt} = \sqrt{\frac{110 \mu_d \omega_s^2 - 225 \omega_s^2}{1342 \beta \mu_b + 1342 \beta \mu_d - 1342 \mu_b - 1342 \mu_d}} \tag{13}$$

Eq. (13) has been inserted into Eq. (12). Therefore, the closed-form expression for the optimal viscous damping ratio of NSIBI has been derived as

$$(\zeta_b)_{opt} = \frac{\sqrt{330}}{220} \sqrt{\frac{(88 \mu_d^2 + 3300 \mu_d - 3375) (1 - \beta)}{(22 \mu_d - 45) (\mu_b + \mu_d)}} \tag{14}$$

The variations of optimal frequency ratio versus base mass ratio have been displayed in Fig. 4(a) for different values of stiffness ratio  $\beta$ . The optimal frequency ratio decreases as the base mass ratio increases, whereas the optimal frequency ratio increases as the stiffness ratio increases. The variations of optimal frequency ratio versus inerter mass ratio have been displayed in Fig. 4(b) for different values of stiffness ratio  $\beta$ . The optimal frequency ratio decreases as the inerter mass ratio increases and increases when the stiffness ratio increases. Therefore, a higher base mass ratio, higher inerter mass ratio, and lower stiffness ratio are recommended to enhance the isolated structures' time period. The extended time period provides additional flexibility to the base of the isolated structures, which increases the dynamic response reduction capacity of the NSIBI. The variations of optimal viscous damping ratio versus base mass ratio have been displayed in Fig. 5(a) for different values of stiffness ratio  $\beta$ . The optimal viscous damping ratio decreases as the base mass ratio increases and decreases as the stiffness ratio increases. The variations of optimal viscous damping ratio versus inerter mass ratio have been displayed in Fig. 5(b) for different values of stiffness ratio  $\beta$ . The optimal viscous damping ratio decreases as the inerter mass ratio increases and decreases as the stiffness ratio increases. However, a lower stiffness ratio provides a lower frequency ratio for the isolated structures, which is essentially required. Therefore, a higher base mass ratio, a higher inerter mass ratio, and a lower stiffness ratio are recommended to design optimal NSIBI for achieving the optimal viscous damping ratio for NSIBI in the affordable range. As a result, the viscous damping ratio stood between 0.1 to 1.0, i.e.,  $0.1 \leq \zeta_b \leq 0.9$ , which is practically implementable and affordable.

### 3.1. Robustness of optimum NSIBI

The  $H_2$  optimized design parameters are applied to the basic mathematical formulations of NSIBI to model the governing system parameters, such as the natural frequency and damping ratio of the novel

isolator, in order to achieve robust dynamic reduction capacity form it subjected to base excitations. The dynamic response of the superstructure is the optimization objective function, which has been minimized using  $H_2$  optimized negative stiffness inerter-based base isolators. The variations of optimal dynamic responses of the top floor of the five-storey building isolated by optimum NSIBI for different values of viscous damping ratio have been shown in Fig. 6. The main structure's damping ratio considers  $\zeta_s = 0.0$ . The base mass ratio for negative stiffness inerter-based base isolator (NSIBI) considers  $\mu_b = 0.80$ , inerter mass ratio  $\mu_d = 0.30$ , stiffness ratio  $\beta = 0.10$ . The considered values for system parameters are substitutes in Eqs. (13) and (14) to obtain the optimal frequency and damping ratio for NSIBI. Therefore, the optimal frequency and damping ratio of NSIBI for frequency domain analysis are determined as 0.38 and 0.58. The total mass ratio for NSIBI derives as  $\mu_b + \mu_d = 0.8 + 0.3 = 1.1$ . The dynamic responses are unrestrained to  $\zeta_b = 0$ , and the response peaks are located at the system's eigen frequencies, i.e.,  $\eta = 0.1385, 0.5506, 1.005, 1.411, 1.729, 1.931$ . The response peaks are shifted from their eigen frequency points when the values of viscous damping ratio are increasing, i.e.,  $\zeta_b \leq 1.0$ . In addition, at  $\eta_{opt} = 0.38$ ,  $(\zeta_b)_{opt} = 0.58$ , the resonating frequencies are extracted from these frequency points. Hence, the resonating frequencies are obtained as  $\eta = 0.1354, 0.5518, 1.059, 1.402, 1.93$ . The dynamic response peaks of the entire isolated structure, having six degrees of freedom system, are merged into five peaks which are the degrees of freedom of superstructure, when the values of viscous damping ratio tend to  $\infty$  (i.e.,  $\zeta_b = \infty$ ) compare to the optimal values. The frequency points for response peaks are located as  $\eta = 0.2827, 0.8326, 1.311, 1.683, 1.919$ . The anti-resonance frequency points are located at  $\eta = 1.0, 1.176, 1.732, 1.902$ . The dynamic response is not significantly minimized after  $(\eta_b)_{opt} = 0.38$ ,  $(\zeta_b)_{opt} = 0.58$  for optimum NSIBI. The robustness of the newly derived optimal closed-form expressions, i.e., Eqs. (13) and (14), have been identified from Fig. 6. The dynamic responses of the multi-storey building have been minimized at its optimal design parameters with affordable ranges.

## 4. Dynamic response evaluation for five-storey buildings

The  $H_2$  optimization method has been performed to derive the optimal closed-form solutions for the design parameters of optimum NSIBI. The optimal dynamic response reduction capacity of NSIBI has been achieved by applying these  $H_2$  optimized optimal closed-form solutions. The dynamic response reduction capacity of optimum conventional base isolators (CBI) has also been determined and compared with the dynamic response reduction capacity of optimum NSIBI. The frequency and time domain analysis have been performed to obtain the exact dynamic response reduction capacity of optimum NSIBI and CBI mathematically.

### 4.1. Frequency domain analysis

The transfer function has been formed to determine analytically the dynamic responses of the five-storey building isolated by optimum CBI and NSIBI subjected to harmonic and random-white noise excitations. The main structure's damping ratio considers  $\zeta_s = 0.01$ . The base mass ratio for negative stiffness inerter-based base isolator (NSIBI) considers  $\mu_b = 0.80$ , inerter mass ratio  $\mu_d = 0.30$ , stiffness ratio  $\beta = 0.10$ . The considered values for system parameters are substitutes in Eqs. (13) and (14) to obtain the optimal frequency and damping ratio for NSIBI. Therefore, the optimal frequency and damping ratio of NSIBI for frequency domain analysis are determined as 0.38 and 0.58. The total mass ratio for NSIBI derives as  $\mu_b + \mu_d = 0.8 + 0.3 = 1.1$ . For the classical base isolator (CBI), the total mass ratio is considered  $\mu_b = 1.1$ , and the frequency and viscous damping ratio for CBI derive as 0.39 and 0.64. Accordingly, all the design parameters for the frequency domain analysis have been listed in Table 1 to provide a better description and evidence for each isolator that the comparison between the solutions is reasonable.

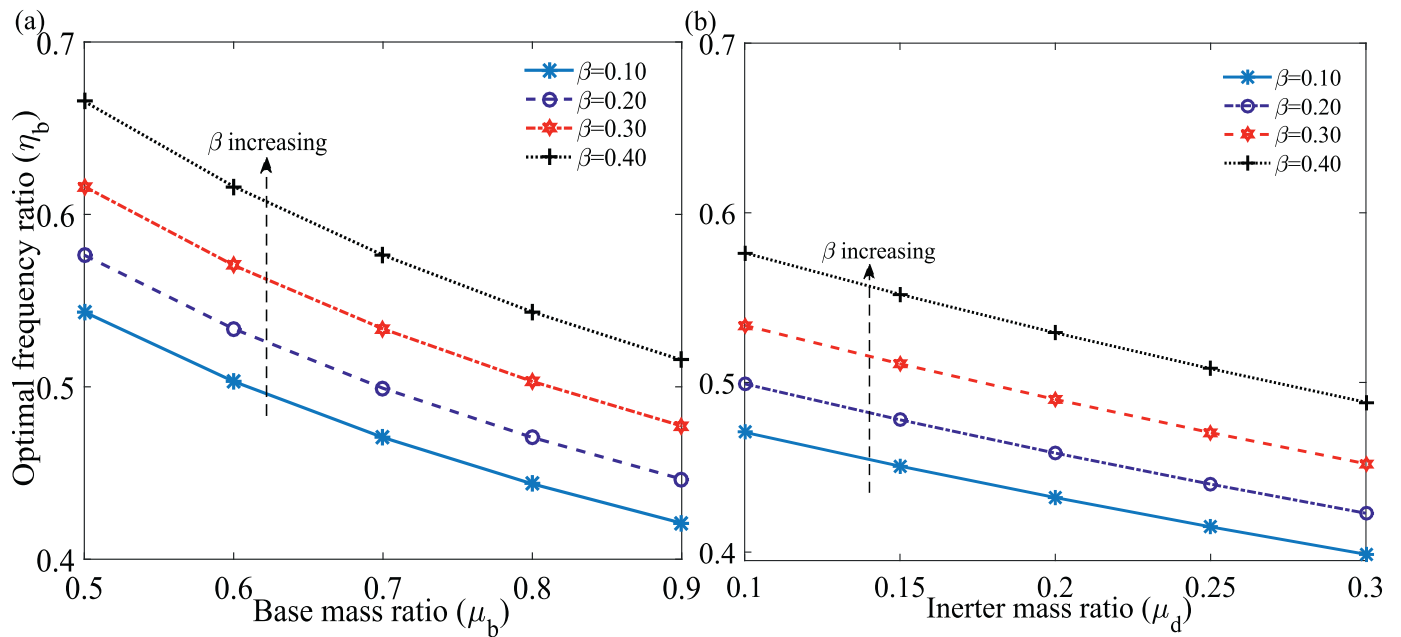


Fig. 4. The variations of optimal frequency ratio versus (a) base mass ratio, (b) inerter mass ratio for different values of stiffness mass ratio.

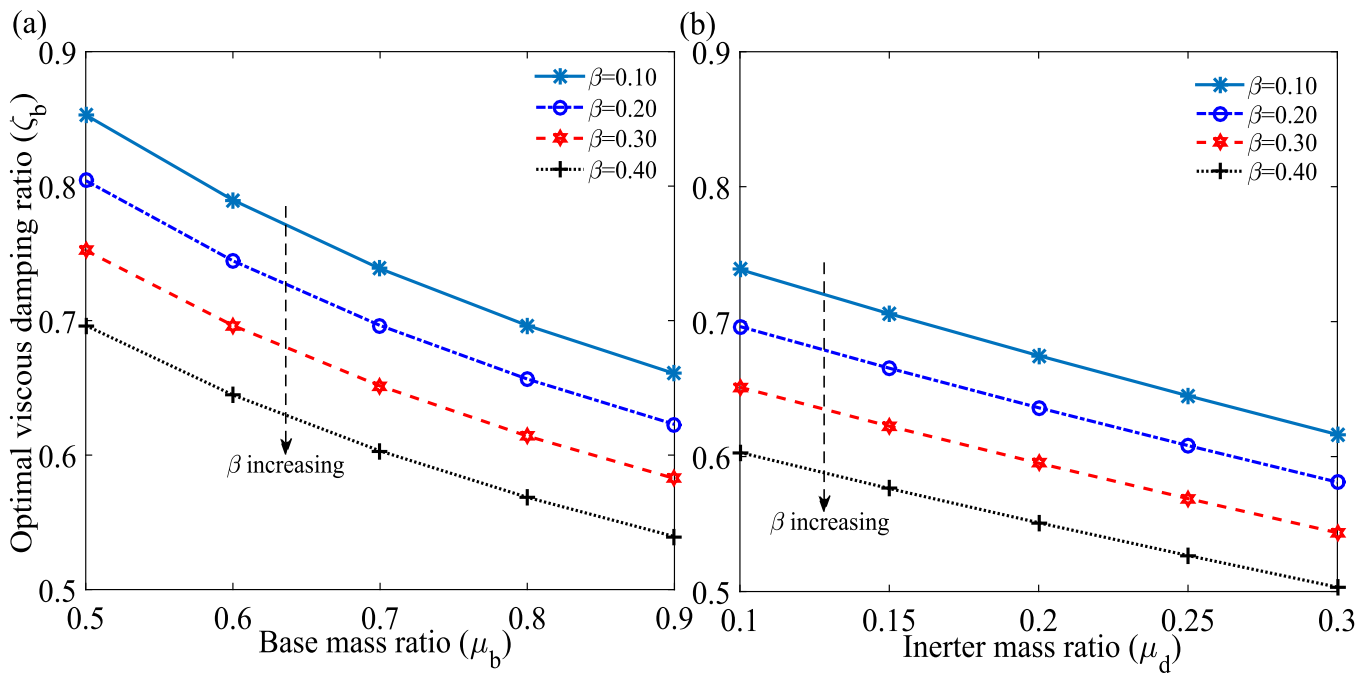


Fig. 5. The variations of optimal viscous damping ratio versus (a) base mass ratio, (b) inerter mass ratio for different values of stiffness mass ratio.

Applying these optimal design parameters, the variations of optimal dynamic responses of the uncontrolled and isolated five-storey buildings versus frequency ratio subjected to harmonic base excitation have been shown in Fig. 7(a). The maximum dynamic response of the top floor of the uncontrolled building obtains as 2714.1. The maximum dynamic responses of the top floor of the buildings isolated by CBI and NSIBI obtain as 92.63 and 44.53. Therefore, the dynamic response reduction capacity of NSIBI is significantly 51.93% superior to the dynamic response reduction capacity of CBI subjected to harmonic excitations. In addition, the variations of optimal dynamic responses of the uncontrolled and isolated five-storey buildings versus frequency ratio subjected to random-white noise excitations have been shown in Fig. 7(b). The maximum dynamic response of the top floor of

the uncontrolled building has been determined as  $1.33 \times 10^{11}$  dB/Hz. The maximum dynamic responses of the top floor of the five-storey building isolated by CBI and NSIBI have been derived as  $1.97 \times 10^8$  dB/Hz and  $3.7 \times 10^7$  dB/Hz. Therefore, the dynamic response reduction capacity of NSIBI is significantly 81.24% superior to the dynamic response reduction capacity of CBI subjected to random-white noise base excitation.

#### 4.2. Time history analysis

The  $H_2$  optimization method applies to derive the exact closed-form expressions for optimal design parameters of optimum NSIBI.

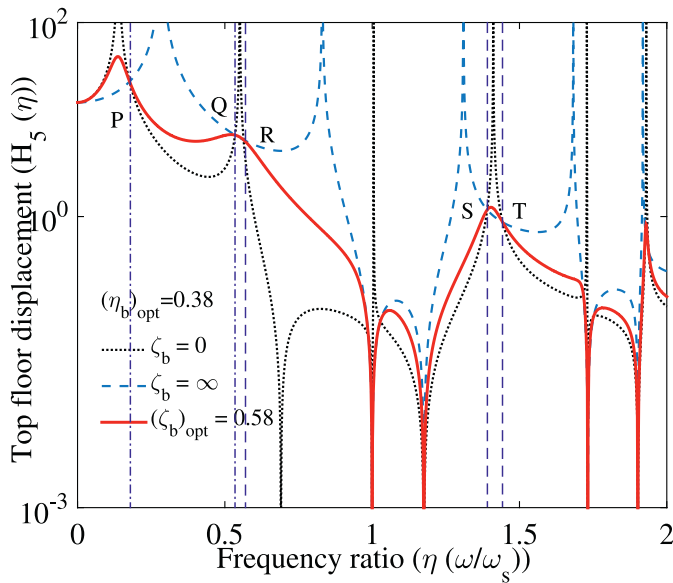


Fig. 6. The variations of optimal dynamic responses of the top floor of the five-storey building isolated by NSIBI versus frequency ratio for different values of viscous damping ratio.

Table 1 The system parameters for non-isolated and isolated multi-storey buildings. Eqs. (13) and (14) have been utilized to determine optimal design parameters for isolators.

Description	Symbol		Value	
	CBI	NSIBI	CBI	NSIBI
Damping ratio of structure	$\zeta_s$	$\zeta_s$	0.01	0.01
Isolator damping ratio	$\zeta_b$	$\zeta_b$	0.64	0.58
Frequency ratio of isolator	$\eta_b$	$\eta_b$	0.39	0.38
Total mass ratio of isolator	$\mu_b$	$\mu_b + \mu_d$	1.1	1.1
Base mass ratio	...	$\mu_b$	0	0.80
Inerter mass ratio	...	$\mu_d$	0	0.30
Stiffness ratio	...	$\beta$	0	0.10

Using these optimal closed-form solutions, the robust dynamic reduction capacity from NSIBI has been achieved in frequency domain analysis. Furthermore, a numerical study has been conducted to verify the accuracy of the  $H_2$  optimized closed-form solutions for the isolators with the time-domain responses, considering the Newmark-beta method. The near-field earthquake records are applied as seismic base excitations to perform the time history analysis and determine time domain responses. The displacement and acceleration response reduction capacities of optimum NSIBI and CBI have been determined through this time history analysis and compared to determine the superior performance between them. Therefore, to perform the numerical study, each floor’s mass considers  $m_s = 3000$  tons; the structural time period considers  $T_s = 0.5$  s, and the natural frequency derives through  $\omega_s = 2\pi/T_s$ . The schematic diagrams of the isolated multi-storey buildings, negative stiffness inerter-based base isolators and conventional base isolators subjected to seismic base excitations are shown in Figs. 8(a), 8(b), and 8(c). The main structure’s damping ratio considers  $\zeta_s = 0.01$ . The base mass ratio for negative stiffness inerter-based base isolator (NSIBI) considers  $\mu_b = 0.80$ , inerter mass ratio  $\mu_d = 0.30$ , stiffness ratio  $\beta = 0.10$ . The considered values for system parameters are substitutes in Eqs. (13) and (14) to obtain the optimal frequency and damping ratio for NSIBI. Therefore, the optimal frequency and damping ratio of NSIBI for frequency domain analysis are determined as 0.38 and 0.58. The total mass ratio for NSIBI derives as  $\mu_b + \mu_d = 0.8 + 0.3 = 1.1$ . For the classical base isolator (CBI), the total mass ratio is considered  $\mu_b = 1.1$ , and the frequency and viscous damping ratio for CBI derive as 0.39 and 0.64. Accordingly, all the design parameters for the time history

Table 2 The system parameters for uncontrolled and isolated multi-storey buildings. Eqs. (13) and (14) have been utilized to determine optimal design parameters for isolators.

Description	Symbol		Value	
	CBI	NSIBI	CBI	NSIBI
Damping ratio of structure	$\zeta_s$	$\zeta_s$	0.01	0.01
Isolator damping ratio	$\zeta_b$	$\zeta_b$	0.64	0.58
Frequency ratio of isolator	$\eta_b$	$\eta_b$	0.39	0.38
Total mass ratio of isolator	$\mu_b$	$\mu_b + \mu_d$	1.1	1.1
Base mass ratio	...	$\mu_b$	0	0.80
Inerter mass ratio	...	$\mu_d$	0	0.30
Stiffness ratio	...	$\beta$	0	0.10

analysis have been listed in Table 2 to provide a better description and evidence for each isolator that the comparison between the solutions is reasonable. In addition, the details of near-field earthquake records are listed in Table 3. The response spectra of all near-field earthquake records (pulse), listed in Table 3, are shown in Fig. 9 with considering 5% damping. Near-field earthquakes (pulse records) are more threatening for the structures compared to far-field earthquakes [34]. Hence, near-field earthquake records with pulses having a noticeable vertical component are applied for the numerical study to investigate the vibration reduction capacity of each isolator. An algorithm for the procedure of optimal dynamic response calculation from time history analysis for the structures isolated by optimum isolators has been displayed in Fig. 10.

Therefore, the variations of top floor displacements of uncontrolled and isolated five-storey buildings versus time subjected to Northridge-01 Chi-Chi, Taiwan earthquake excitation have been shown in Fig. 11(a). The maximum displacement of the top floor of the uncontrolled buildings and buildings isolated by CBI, NSIBI subjected to the Northridge-01 earthquake have been obtained as 0.0947 m, 0.0720 m, and 0.0263 m. The variations of top floor displacements of uncontrolled and isolated five-storey buildings versus time subjected to Chi-Chi, Taiwan earthquake excitation have been shown in Fig. 11(b). The maximum displacement of the top floor of the uncontrolled buildings and buildings isolated by CBI, NSIBI subjected to Chi-Chi, Taiwan earthquake excitation have been obtained as 0.1101 m, 0.0657 m, and 0.03 m. The maximum displacement of the top floor of uncontrolled and isolated buildings and the displacement response reduction capacity of NSIBI w.r.t CBI ( $D_5$  (%)) for five-storey buildings subjected to near-field earthquake base excitations are listed in Table 4. The mathematical formulation to determine the displacement response reduction capacity of NSIBI w.r.t CBI ( $D_5$  (%)) for five-storey buildings derives as

$$D_5 (\%) = \frac{(x_5^{max})_{CBI} - (x_5^{max})_{NSIBI}}{(x_5^{max})_{CBI}} \tag{15}$$

The variations of top-floor accelerations of uncontrolled and isolated five-storey buildings versus time subjected to Northridge-01 earthquake excitations have been shown in Fig. 12(a). The maximum accelerations of the top floor of the uncontrolled buildings and buildings isolated by CBI, NSIBI subjected to the Northridge-01 earthquake excitation have been obtained as 2.2652 m/s<sup>2</sup>, 1.7506 m/s<sup>2</sup>, and 0.8167 m/s<sup>2</sup>.

The variations of top-floor accelerations of uncontrolled and isolated five-storey buildings versus time subjected to the Chi-Chi, Taiwan earthquake excitation have been shown in Fig. 12(b). The maximum accelerations of the top floor of the uncontrolled buildings and buildings isolated by CBI, NSIBI subjected to Chi-Chi, Taiwan earthquake excitation have been obtained as 1.9879 m/s<sup>2</sup>, 0.8347 m/s<sup>2</sup>, and 0.516 m/s<sup>2</sup>. The maximum acceleration of the top floor of uncontrolled and isolated buildings and the acceleration response reduction capacity of NSIBI w.r.t CBI ( $A_5$  (%)) for five-storey buildings subjected to near-field earthquake ground motions are listed in Table 5. The mathematical

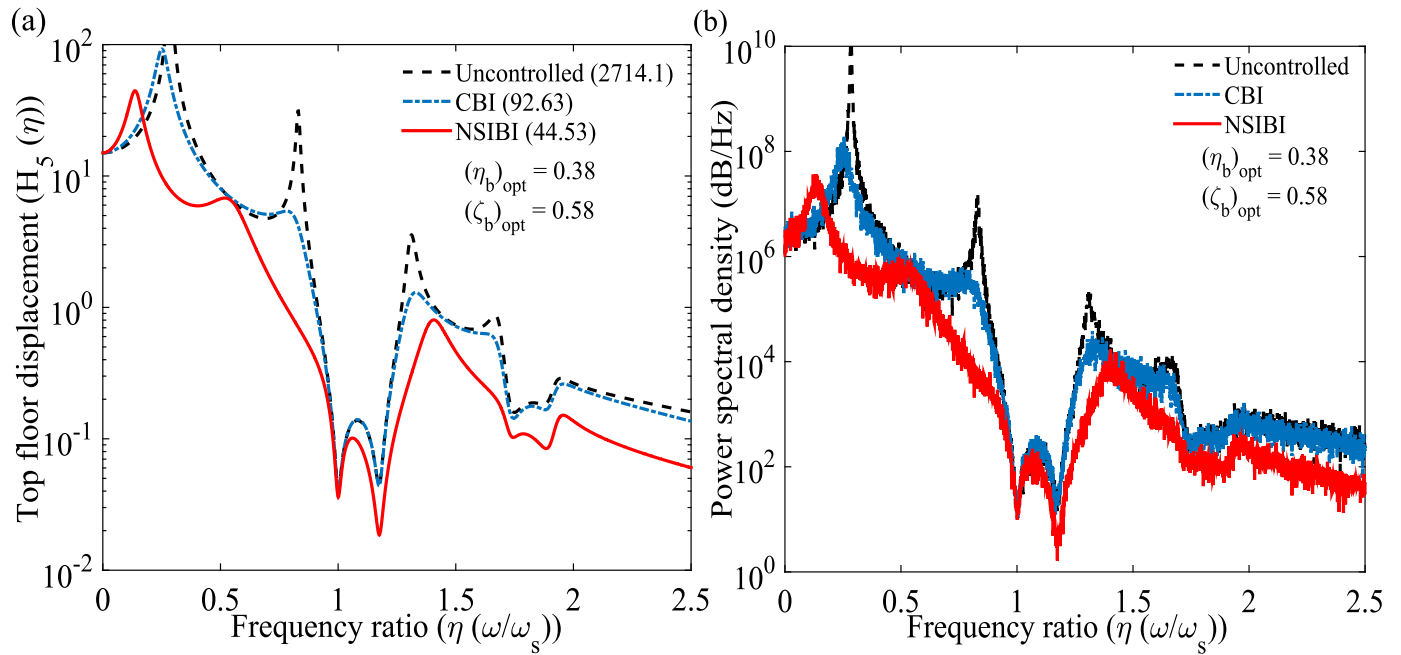


Fig. 7. The variations of optimal dynamic responses of non-isolated and isolated five-storey buildings versus frequency ratio subjected to (a) harmonic and (b) random-white noise base excitations.

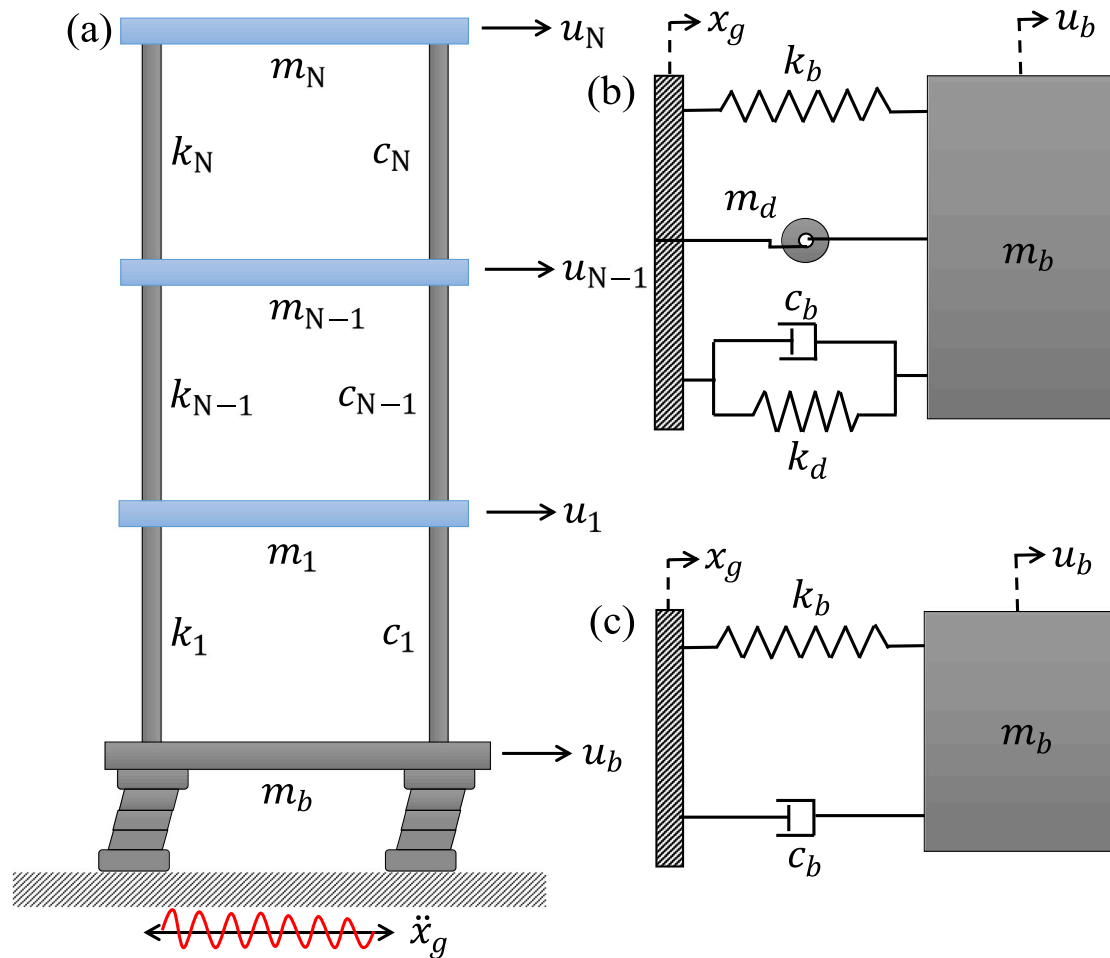


Fig. 8. The schematic diagrams of the (a) isolated multi-storey buildings, (b) negative stiffness inerter-based base isolators, and (c) conventional base isolators subjected to base excitations.

**Table 3**  
The details of near-field earthquake base excitations (pulse records) (<https://peer.berkeley.edu/peer-strong-ground-motion-databases>).

Earthquake	Year	$M_w$	Recording station	$V_{s30}$ (m/s)	Component	$E_s$ (km)	PGA,g
Irpinia, Italy-01	1980	6.9	Sturmo	1000	MUL009	30.4	0.31
Superstition Hills-02	1987	6.5	Parachute Test Site	349	SUPERST	16.0	0.42
Loma Prieta	1989	6.9	LOMAP	371	HEC000	27.2	0.38
Erzican, Turkey	1992	6.7	Erzincan 11	275	ERZIKAN	9.0	0.49
Cape Mendocino	1992	7.0	CAPEMEND	713	NIS090	4.5	0.63
Landers	1992	7.3	Lucerne	685	LANDERS	44.0	0.79
Northridge-01	1994	6.7	Rinaldi Receiving Sta	282	NORTHR	10.9	0.87
Kocaeli, Turkey	1999	7.5	Izmit	811	KOCAELI	5.3	0.22
Chi-Chi, Taiwan	1999	7.6	TCU065	306	CHICHI	26.7	0.82
Chi-Chi, Taiwan	1999	7.6	TCU102	714	CHICHI	45.6	0.29
Duzce, Turkey	1999	7.1	Duzce	276	DUZCE	1.6	0.52

**Table 4**  
The maximum displacement of top floor of uncontrolled and isolated buildings and the displacement response reduction capacity of NSIBI w.r.t CBI ( $D_5$  (%)) for five-storey buildings.

Earthquake	$x_5^{max}$ (m)		$D_5$ (%)	
	Uncontrolled	CBI	NSIBI	NSIBI
Irpinia, Italy-01	0.0456	0.0246	0.0111	54.88
Superstition Hills-02	0.0475	0.0318	0.0122	61.64
Loma Prieta	0.0577	0.0297	0.0139	53.20
Erzican, Turkey	0.0844	0.0594	0.0217	63.47
Cape Mendocino	0.0512	0.0378	0.0173	54.23
Landers	0.0238	0.0154	0.0046	70.13
Northridge-01	0.0947	0.072	0.0263	63.47
Kocaeli, Turkey	0.0323	0.0133	0.006	54.89
Chi-Chi, Taiwan	0.1101	0.0657	0.03	54.34
Chi-Chi, Taiwan	0.0605	0.0428	0.0203	52.57
Duzce, Turkey	0.0525	0.0359	0.0177	50.70
Average	0.060	0.039	0.016	57.591

**Table 5**  
The maximum acceleration of top floor of uncontrolled and isolated buildings and the acceleration response reduction capacity of NSIBI w.r.t CBI ( $A_5$  (%)) for five-storey buildings.

Earthquake	$\ddot{x}_5^{max}$ (m/s <sup>2</sup> )			$A_5$ (%)
	Uncontrolled	CBI	NSIBI	NSIBI
Irpinia, Italy-01	0.6848	0.3225	0.1232	61.80
Superstition Hills-02	0.8661	0.6269	0.2268	63.82
Loma Prieta	0.8702	0.6544	0.3049	53.41
Erzican, Turkey	1.4185	1.1978	0.5425	54.71
Cape Mendocino	1.5316	1.0531	0.4666	55.69
Landers	0.8793	0.5861	0.2914	50.28
Northridge-01	2.2652	1.7506	0.8167	53.35
Kocaeli, Turkey	0.6358	0.3054	0.1232	59.66
Chi-Chi, Taiwan	1.9879	0.8347	0.516	38.18
Chi-Chi, Taiwan	0.8452	0.5188	0.1534	70.43
Duzce, Turkey	1.1639	0.8211	0.4266	48.05
Average	1.195	0.788	0.363	55.398

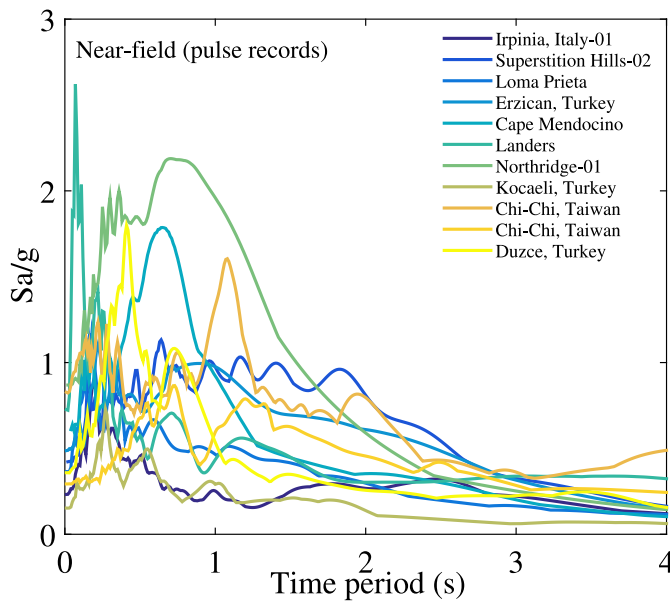


**Fig. 9.** The response spectra of near-field earthquake base excitations (pulse records) (5% damping).

formulation to determine the acceleration response reduction capacity of NSIBI w.r.t CBI ( $A_5$  (%)) for five-storey buildings derives as

$$A_5 (\%) = \frac{(\ddot{x}_5^{max})_{CBI} - (\ddot{x}_5^{max})_{NSIBI}}{(\ddot{x}_5^{max})_{CBI}} \quad (16)$$

The bar diagram of the normalized maximum displacement of the main structure’s top floor subjected to near-field earthquake base excitations has been shown in Fig. 13(a). The bar plot for the optimum

NSIBI-isolated structure’s displacement profile is comparatively less than the bar plot of the displacement profile of structures isolated by optimum CBI. Therefore, the displacement reduction capacity of the optimum NSIBI is significantly more than the optimum CBI. The bar diagram of the normalized maximum acceleration of the main structure’s top floor subjected to near-field earthquake base excitations has been shown in Fig. 13(b). The bar plot for the optimum NSIBI-isolated structure’s acceleration profile is comparatively less than the bar plot of the acceleration profile of structures isolated by optimum CBI. Therefore, the acceleration reduction capacity of the optimum NSIBI is significantly more than the optimum CBI. The variations of normalized damping force of uncontrolled and isolated structures for Northridge-01 earthquake excitations have been displayed in Fig. 14(a). In addition, the variations of normalized damping force of uncontrolled and isolated structures for Chi-Chi, Taiwan earthquake excitations have been displayed in Fig. 14(b). The peaks of the damping force of the top floor of the building isolated by NSIBI are less than the damping forces of the top floor of the uncontrolled building and building isolated by CBI. Therefore, the damping force reduction capacity of NSIBI is significantly superior to the CBI. The maximum displacement of each floor has been determined. Hence, the variations of maximum displacement of each floor versus floor number of the five-storey buildings subjected to Northridge-01 earthquake base excitations have been shown in Fig. 15(a), and for Chi-Chi, Taiwan earthquake has been shown in Fig. 15(b). For all cases, the maximum displacement of each floor is significantly less than that of uncontrolled buildings and building isolated by CBI. The maximum acceleration of each floor has also been determined. Therefore, the variations of maximum acceleration of each floor versus floor number of the five-storey buildings subjected to Northridge-01 earthquake base excitation have been displayed in Fig. 16(a), and for Chi-Chi, Taiwan earthquake has been shown in Fig. 16(b). Each floor acceleration of a building isolated by NSIBI is significantly less than the building isolated by CBI and uncontrolled

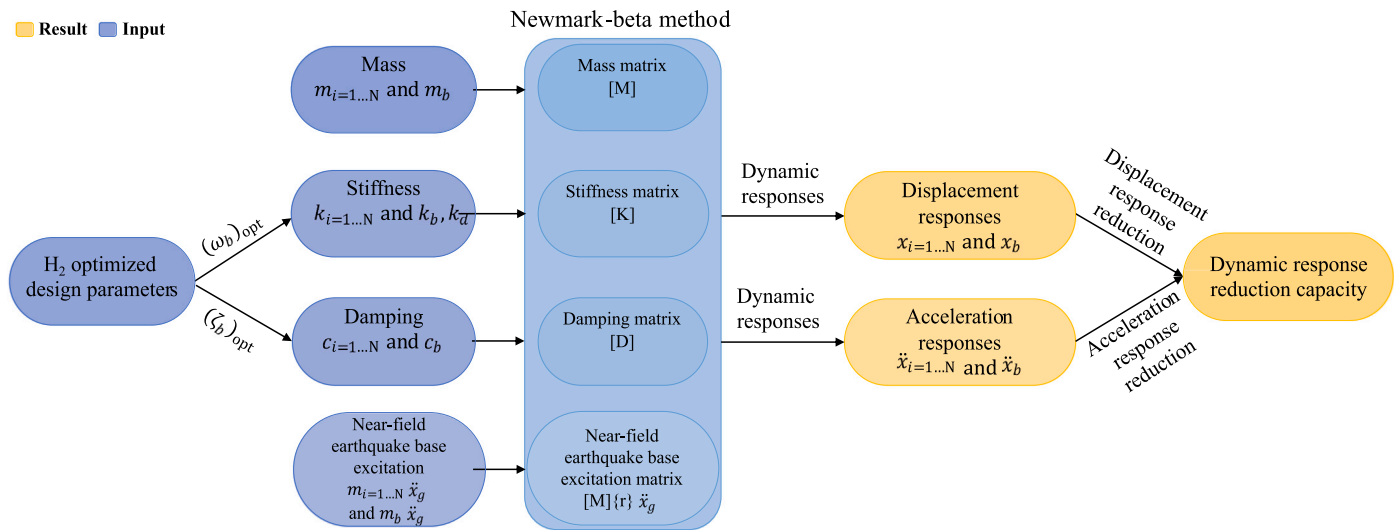


Fig. 10. An algorithm for the procedure of optimal dynamic response calculation from time history analysis.

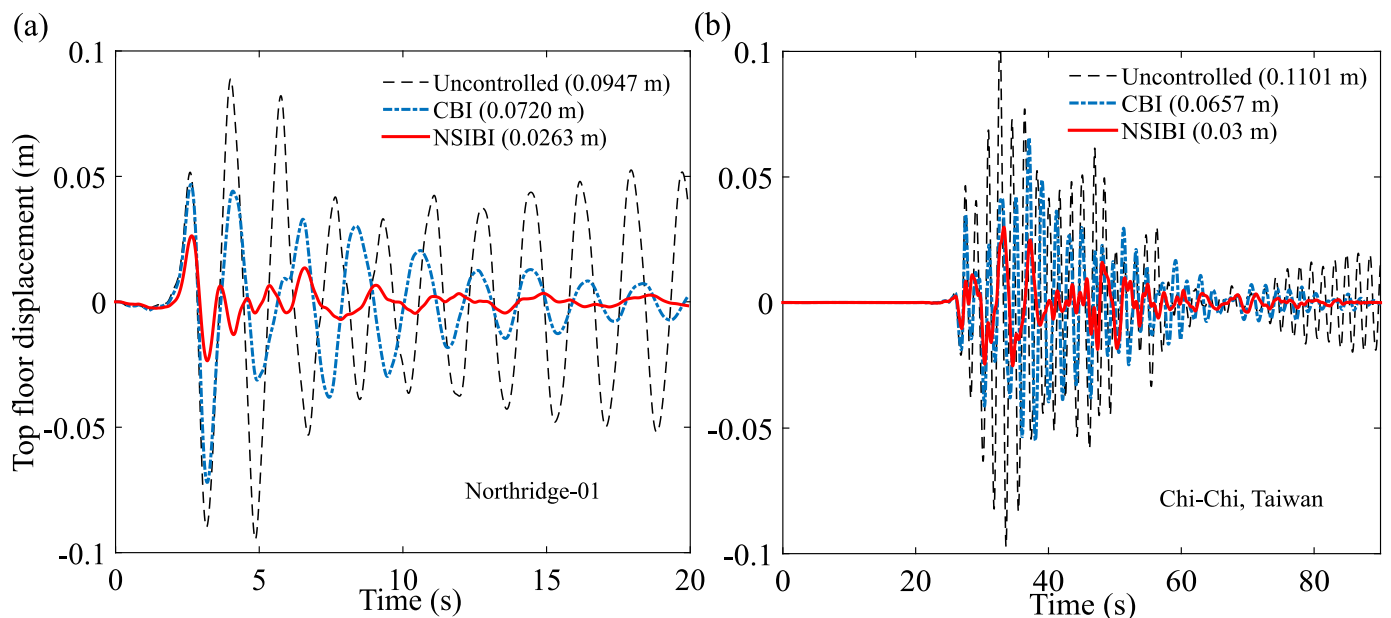


Fig. 11. The variations of top floor displacements of uncontrolled and isolated five storey buildings versus time subjected to (a) Northridge-01 and (b) Chi-Chi, Taiwan earthquake base excitations.

building. Therefore, the  $H_2$  optimized NSIBI has more dynamic response reduction capacity for both cases than the  $H_2$  optimized CBI. The variations of kinetic, potential, and dissipated energy of the uncontrolled structure versus time subjected to Northridge-01 earthquake base excitation have been shown in Fig. 17, structure isolated by CBI, and structure isolated by NSIBI have been shown in Fig. 17(b) and Fig. 17(c). The energy profiles of the uncontrolled structure and structure isolated by CBI is much more than that of the structure isolated by NSIBI. The energy profile of both isolators has also been determined. Therefore, the variations of the kinetic, potential, and dissipated energy profile of the CBI subjected to Northridge-01 earthquake base excitation have been shown in Fig. 18(a) and the energy profile of the NSIBI has been shown in Fig. 18(b). The energy dissipation capacity of the NSIBI is significantly greater than the energy dissipation capacity of CBI.

### 5. Dynamic response evaluation for ten-storey building

The optimal dynamic response reduction capacities of optimum NSIBI and CBI have also been achieved analytically and numerically

for ten-storey buildings to find out the exact performance of novel NSIBI and its superiority over CBI. To obtain the exact superior performance of optimum NSIBI, the dynamic response reduction capacity of optimum NSIBI has also been compared with the dynamic response reduction capacity of optimum CBI. The frequency and time domain analysis have been performed to obtain these results analytically and numerically. The transfer function has been formed to determine analytically the dynamic responses of the ten-storey building isolated by optimum CBI and NSIBI subjected to harmonic and random-white noise excitations.

#### 5.1. Robustness of optimum NSIBI

The variations of optimal dynamic responses of the top floor of the ten-storey building isolated by optimum NSIBI for different values of viscous damping ratio have been shown in Fig. 19. The main structure's damping ratio considers  $\zeta_s = 0.0$ . The base mass ratio for negative stiffness inerter-based base isolator (NSIBI) considers  $\mu_b = 0.80$ , inerter

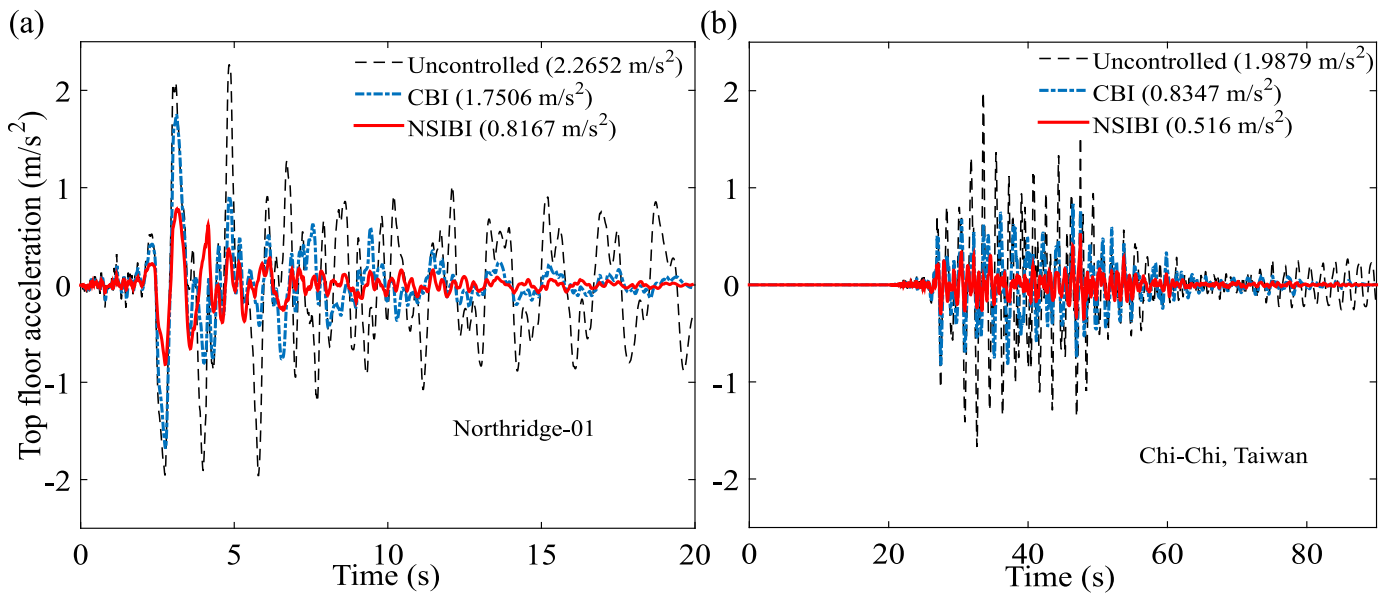


Fig. 12. The variations of top floor accelerations of uncontrolled and isolated five storey buildings versus time subjected to (a) Northridge-01 and (b) Chi-Chi, Taiwan earthquake base excitations.

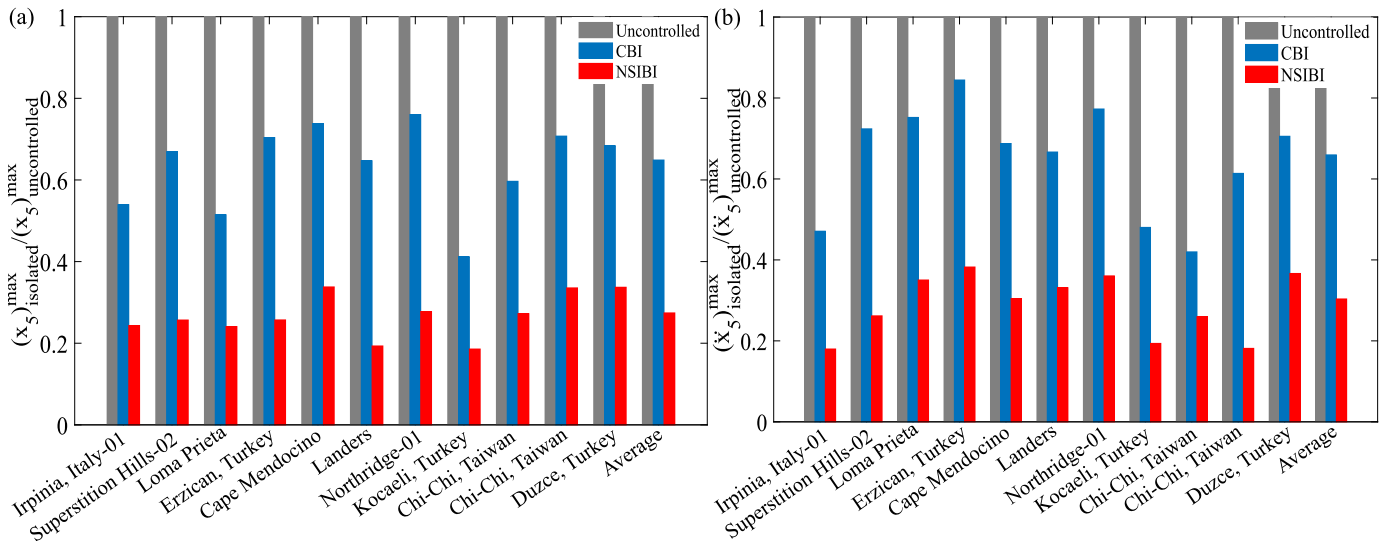


Fig. 13. The bar diagrams of normalized (a) maximum displacement and (b) maximum acceleration of the main structure's top floor subjected to near-field earthquake base excitations.

mass ratio  $\mu_d = 0.30$ , stiffness ratio  $\beta = 0.10$ . The optimal frequency and damping ratio of NSIBI for frequency domain analysis are considered as  $(\eta_b)_{opt} = 0.3802$ , and  $(\zeta_b)_{opt} = 0.5876$ . The dynamic responses are unrestrained to  $\zeta_b = 0$ , and the response peaks are located at the system's eigen frequencies, i.e.,  $\eta = 0.09307, 0.3216, 0.5799, 0.8376, 1.083, 1.309, 1.509, 1.68, 1.818, 1.918, 1.979$ . The response peaks are shifted from their eigen frequency points when the values of viscous damping ratio are increasing, i.e.,  $\zeta_b \leq 1.0$ . The resonating frequencies are extracted from these frequency points. Hence, the resonating frequencies are obtained as  $\eta = 0.09533, 0.318, 0.8292, 1.299, 1.675, 1.917$ . The dynamic response peaks of the entire isolated structure, having eleven degrees of freedom system, are merged into ten peaks which are the degrees of freedom of superstructure, when the values of viscous damping ratio tend to  $\infty$  (i.e.,  $\zeta_b = \infty$ ) compare to the optimal values. The frequency points for response peaks are located as  $\eta = 0.1495, 0.4453, 0.7307, 1.0, 1.247, 1.466, 1.653, 1.802, 1.911, 1.978$ . The anti-resonance frequency points are located at  $\eta = 0.5635, 0.618, 1.081, 1.176, 1.512, 1.618, 1.819, 1.902, 1.98$ .

### 5.2. Frequency domain analysis

The main structure's damping ratio considers  $\zeta_s = 0.01$ . The base mass ratio for negative stiffness inerter-based base isolator (NSIBI) considers  $\mu_b = 0.80$ , inerter mass ratio  $\mu_d = 0.30$ , stiffness ratio  $\beta = 0.10$ . The optimal frequency and damping ratio of NSIBI for frequency domain analysis are considered as  $(\eta_b)_{opt} = 0.3802$ , and  $(\zeta_b)_{opt} = 0.5876$ . The total mass ratio for NSIBI derives as  $\mu_b + \mu_d = 0.8 + 0.3 = 1.1$ . For the classical base isolator (CBI), the total mass ratio is considered  $\mu_b = 1.1$ , and the frequency and viscous damping ratio for CBI derive as 0.39 and 0.64. The variations of optimal dynamic responses of the uncontrolled and isolated ten-storey buildings versus frequency ratio subjected to harmonic base excitation have been shown in Fig. 20(a). The maximum dynamic response of the top floor of the uncontrolled building has been determined as 18979. The maximum dynamic responses of the top floor of buildings isolated by CBI and NSIBI have been determined as 1316 and 293. Therefore, the dynamic response reduction capacity of NSIBI is significantly 77.73% superior to the dynamic response reduction

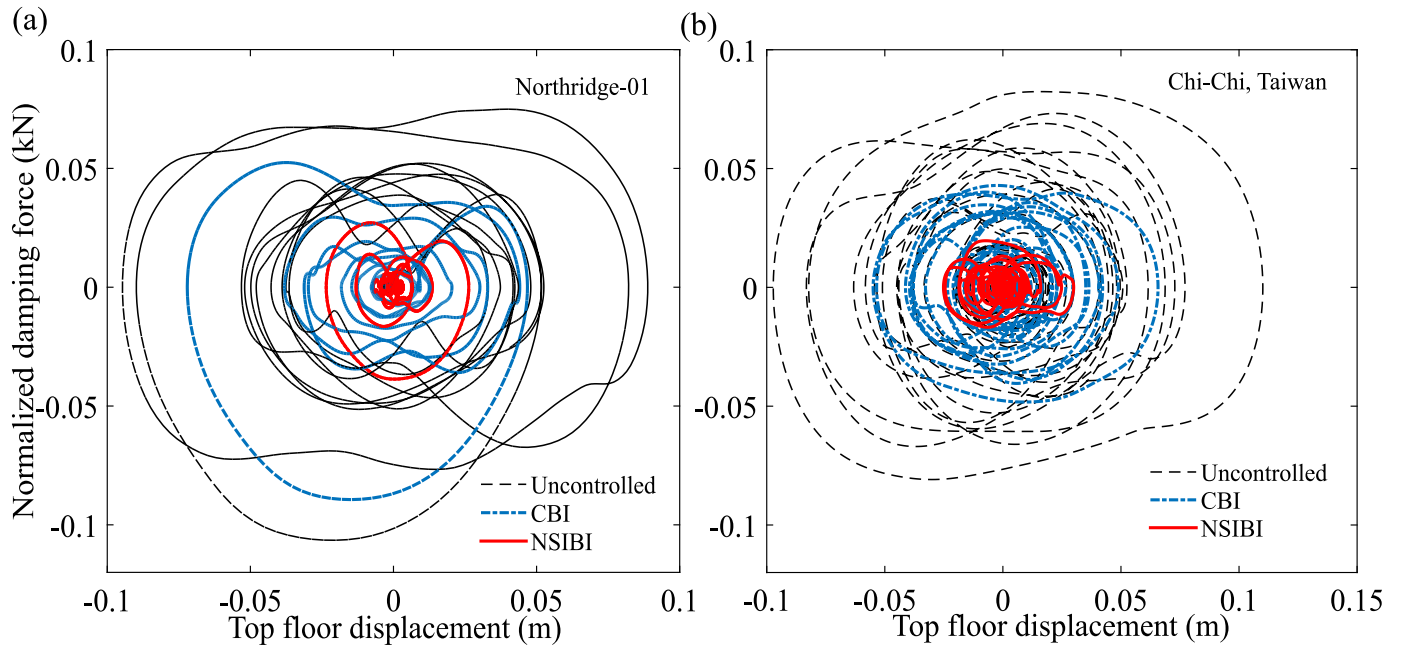


Fig. 14. The variations of normalized damping force versus top floor displacement of the top floor of isolated buildings subjected to (a) Northridge-01 and (b) Chi-Chi, Taiwan earthquake base excitations.

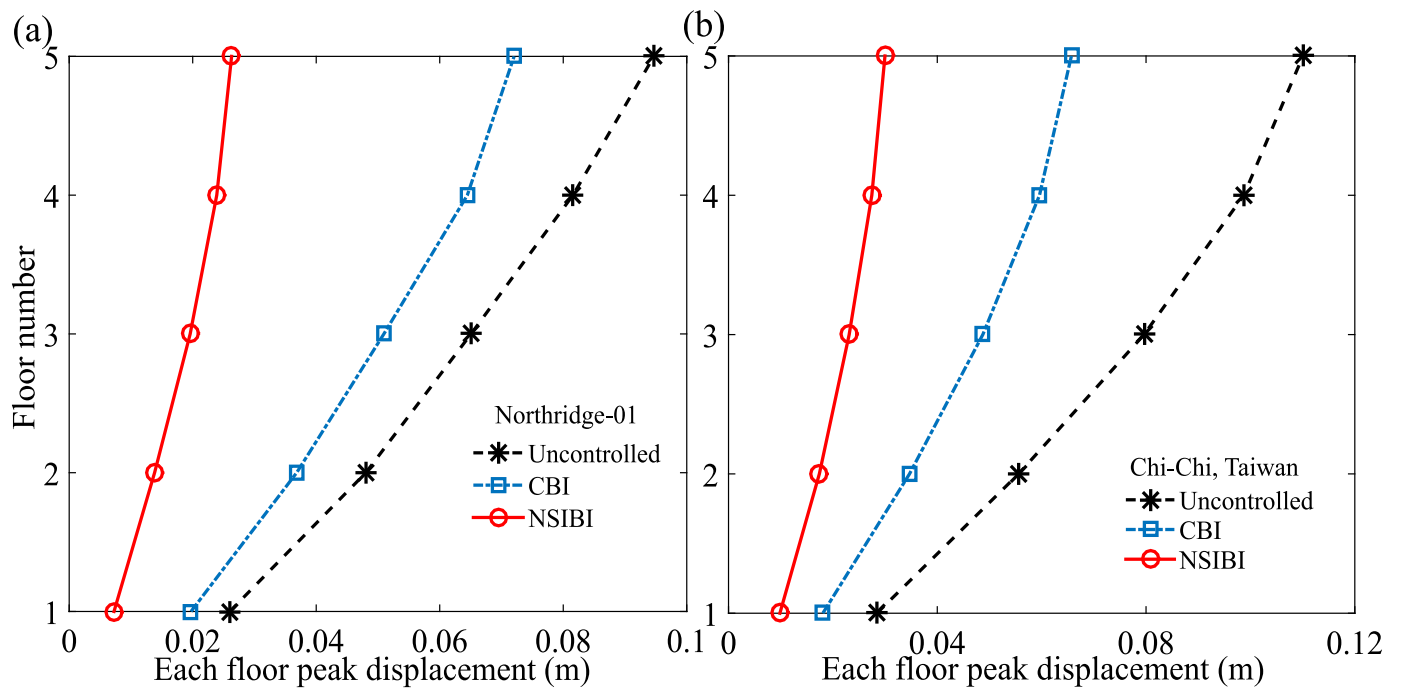


Fig. 15. The variations of peak displacement of each floor versus floor number of the five-storey buildings subjected to (a) Northridge-01 and (b) Chi-Chi, Taiwan earthquake base excitations.

capacity of CBI subjected to harmonic excitations. The variations of optimal dynamic responses of the uncontrolled and isolated ten-storey buildings versus frequency ratio subjected to random-white noise excitations have been shown in Fig. 20(b). The maximum dynamic response of the top floor of the uncontrolled building has been determined as  $3.1885 \times 10^{10}$  dB/Hz. The maximum dynamic responses of the top

floor of the five-storey buildings isolated by CBI and NSIBI have been determined as  $8.6388 \times 10^8$  dB/Hz and  $5.1671 \times 10^7$  dB/Hz. Therefore, the dynamic response reduction capacity of NSIBI is significantly 94.02% superior to the dynamic response reduction capacity of CBI subjected to random-white noise base excitation.

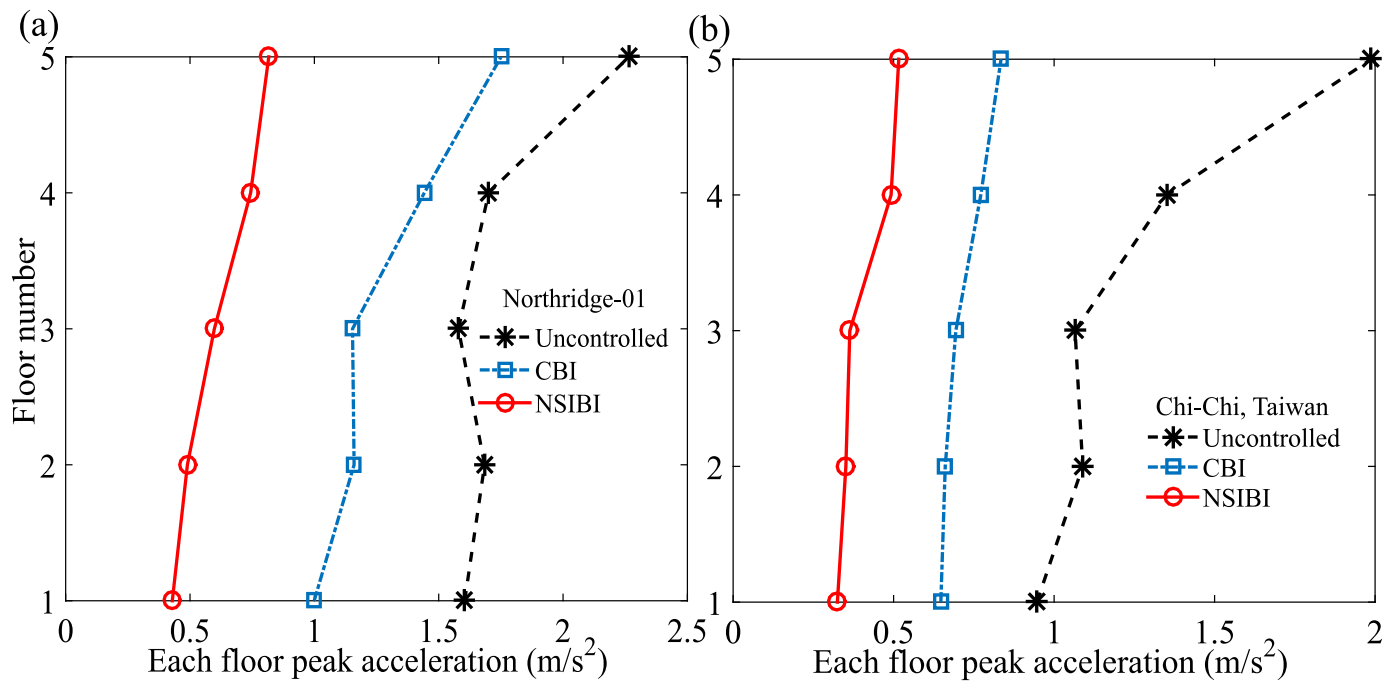


Fig. 16. The variations of peak acceleration of each floor versus floor number of the five-storey buildings subjected to (a) Northridge-01 and (b) Chi-Chi, Taiwan earthquake base excitations.

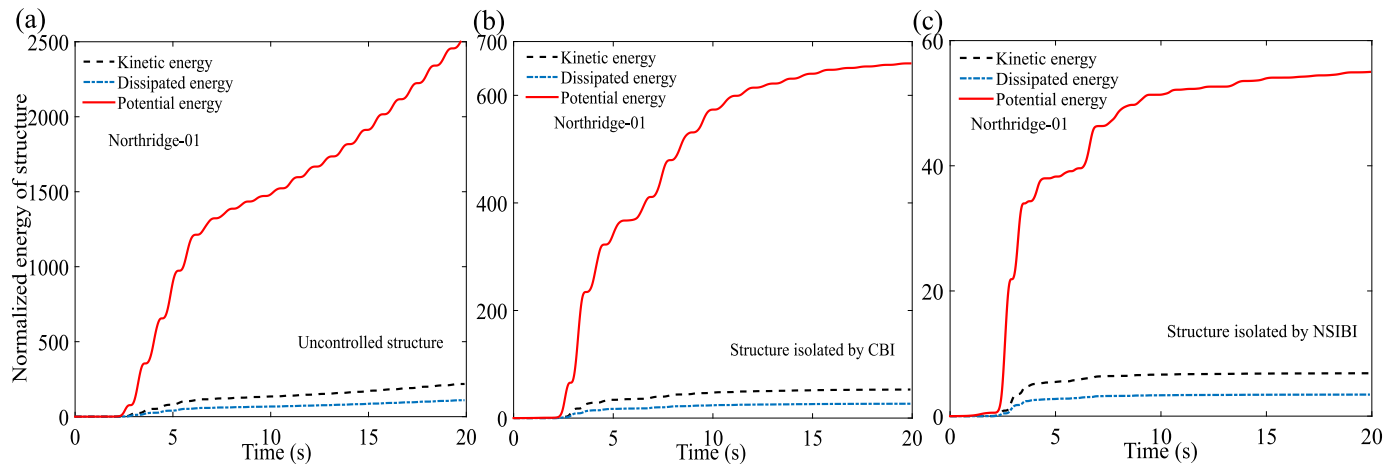


Fig. 17. The variations of kinetic, potential, and dissipated energy of the (a) uncontrolled structure, (b) structure isolated by CBI, and (c) structure isolated by NSIBI versus time subjected to Northridge-01 earthquake base excitation.

### 5.3. Time history analysis

The  $H_2$  optimization method applies to derive the exact closed-form expressions for optimal design parameters of optimum NSIBI. Using these optimal closed-form solutions, the robust dynamic reduction capacity from NSIBI has been achieved in frequency domain analysis. Furthermore, a numerical study has been conducted to verify the accuracy of the  $H_2$  optimized closed-form solutions for the isolators with the time-domain responses, considering the Newmark-beta method. The near-field earthquake records are applied as seismic base excitations to perform the time history analysis and determine time domain responses. The displacement and acceleration response reduction capacities of optimum NSIBI and CBI have been determined through this time history analysis and compared to determine the superior performance between them. Therefore, to perform the numerical study, each floor's mass considers  $m_s = 3000$  tons; the structural time period considers  $T_s = 0.5$  s, and the natural frequency derives through  $\omega_s =$

$2\pi/T_s$ . The schematic diagrams of the isolated multi-storey buildings, negative stiffness inerter-based base isolators and conventional base isolators subjected to seismic base excitations are shown in Figs. 8(a), 8(b), and 8(c). The main structure's damping ratio considers  $\zeta_s = 0.01$ . The base mass ratio for negative stiffness inerter-based base isolator (NSIBI) considers  $\mu_b = 0.80$ , inerter mass ratio  $\mu_d = 0.30$ , stiffness ratio  $\beta = 0.10$ . The optimal frequency and damping ratio of NSIBI for frequency domain analysis are considered as  $(\eta_b)_{opt} = 0.3802$ , and  $(\zeta_b)_{opt} = 0.5876$ . The total mass ratio for NSIBI derives as  $\mu_b + \mu_d = 0.8 + 0.3 = 1.1$ . For the classical base isolator (CBI), the total mass ratio is considered  $\mu_b = 1.1$ , and the frequency and viscous damping ratio for CBI derive as 0.39 and 0.64. The variations of top floor displacements of uncontrolled and isolated ten storey buildings versus time subjected to Northridge-01 earthquake base excitation have been shown in Fig. 21(a). The maximum displacement of top floor of the uncontrolled buildings and buildings isolated by CBI, NSIBI subjected to Northridge-01 earthquake have been obtained as 0.0902 m, 0.0592 m,

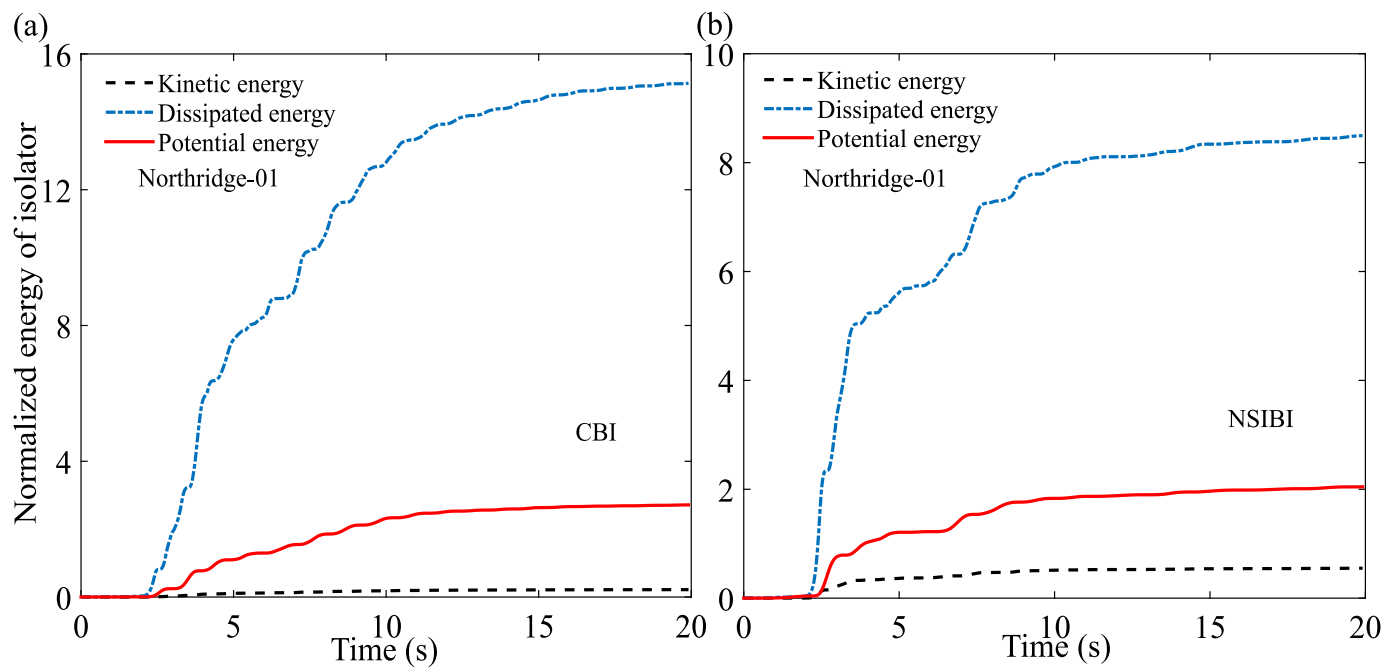


Fig. 18. The variations of kinetic, potential, and dissipated energy profile of the CBI and NSIBI versus time subjected to Northridge-01 earthquake base excitation.

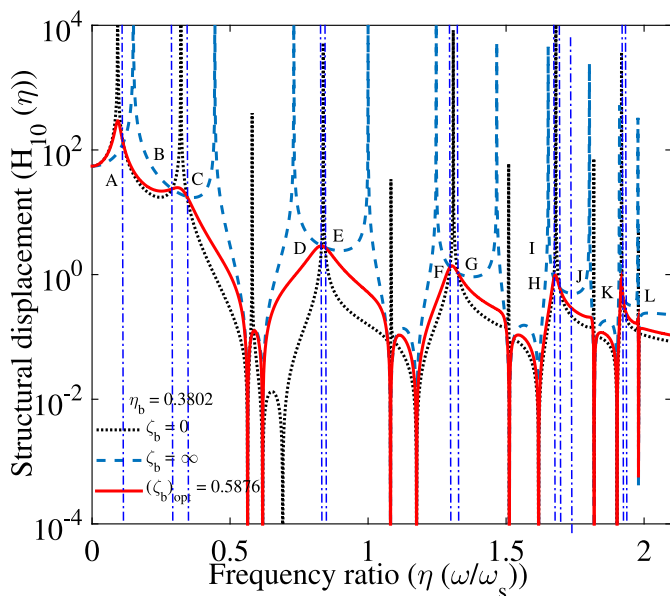


Fig. 19. The variations of optimal dynamic responses of the top floor of ten storey building versus frequency ratio for different values of viscous damping ratio of NSIBI.

and 0.0297 m. The maximum displacement of each floor has been determined. Hence, the variations of maximum displacement of each floor versus floor number of the ten-storey buildings subjected to Northridge-01 earthquake base excitations have been shown in Fig. 21(b). The maximum displacement of each floor is significantly less than that of uncontrolled buildings and building isolated by CBI. The maximum displacement of top floor of uncontrolled ten-storey and isolated ten-storey buildings and the displacement response reduction capacity of NSIBI w.r.t CBI ( $D_{10}$  (%)) for ten-storey buildings subjected to near-field earthquake ground motions are listed in Table 6. The mathematical formulation to determine the displacement response reduction capacity

Table 6

The maximum displacement of top floor of uncontrolled and isolated buildings and the displacement response reduction capacity of NSIBI w.r.t CBI ( $D_{10}$  (%)) for ten-storey buildings.

Earthquake	$x_{10}^{max}$ (m)			$D_r$ (%)
	Uncontrolled	CBI	NSIBI	
Irpinia, Italy-01	0.0913	0.0807	0.0286	64.56
Superstition Hills-02	0.1721	0.1443	0.0498	65.49
Loma Prieta	0.1195	0.0837	0.034	59.38
Erzican, Turkey	0.0756	0.0716	0.0371	48.18
Cape Mendocino	0.0689	0.0589	0.0308	47.71
Landers	0.2324	0.2137	0.1156	45.91
Northridge-01	0.0902	0.0592	0.0297	49.83
Kocaeli, Turkey	0.0244	0.0222	0.0123	44.59
Chi-Chi, Taiwan	0.2973	0.2586	0.1101	57.42
Chi-Chi, Taiwan	0.3249	0.2468	0.0825	66.57
Duzce, Turkey	0.2746	0.2134	0.062	70.95
Average	0.161	0.132	0.054	56.42

of NSIBI w.r.t CBI ( $D_{10}$  (%)) for ten-storey buildings derives as

$$D_{10} (\%) = \frac{(x_{10}^{max})_{CBI} - (x_{10}^{max})_{NSIBI}}{(x_{10}^{max})_{CBI}} \quad (17)$$

The variations of top floor accelerations of uncontrolled and isolated ten-storey buildings versus time subjected to Northridge-01 earthquake base excitations have been shown in Fig. 22(a). The maximum accelerations of the top floor of the uncontrolled buildings and buildings isolated by CBI, NSIBI subjected to the Northridge-01 earthquake have been obtained as 1.4699  $m/s^2$ , 1.2898  $m/s^2$ , and 0.4985  $m/s^2$ . The maximum acceleration of each floor has also been determined. Therefore, the variations of maximum acceleration of each floor versus floor number of the ten-storey buildings subjected to Northridge-01 earthquake base excitation have been displayed in Fig. 22(b). Each floor acceleration of a building isolated by NSIBI is significantly less than the building isolated by CBI and uncontrolled building. Therefore, the  $H_2$  optimized NSIBI has more dynamic response reduction capacity for both cases than the  $H_2$  optimized CBI. The maximum acceleration of the top floor of uncontrolled and isolated buildings and the acceleration response reduction capacity of NSIBI w.r.t CBI ( $A_{10}$  (%)) for ten-storey buildings subjected to near-field earthquake ground motions are listed

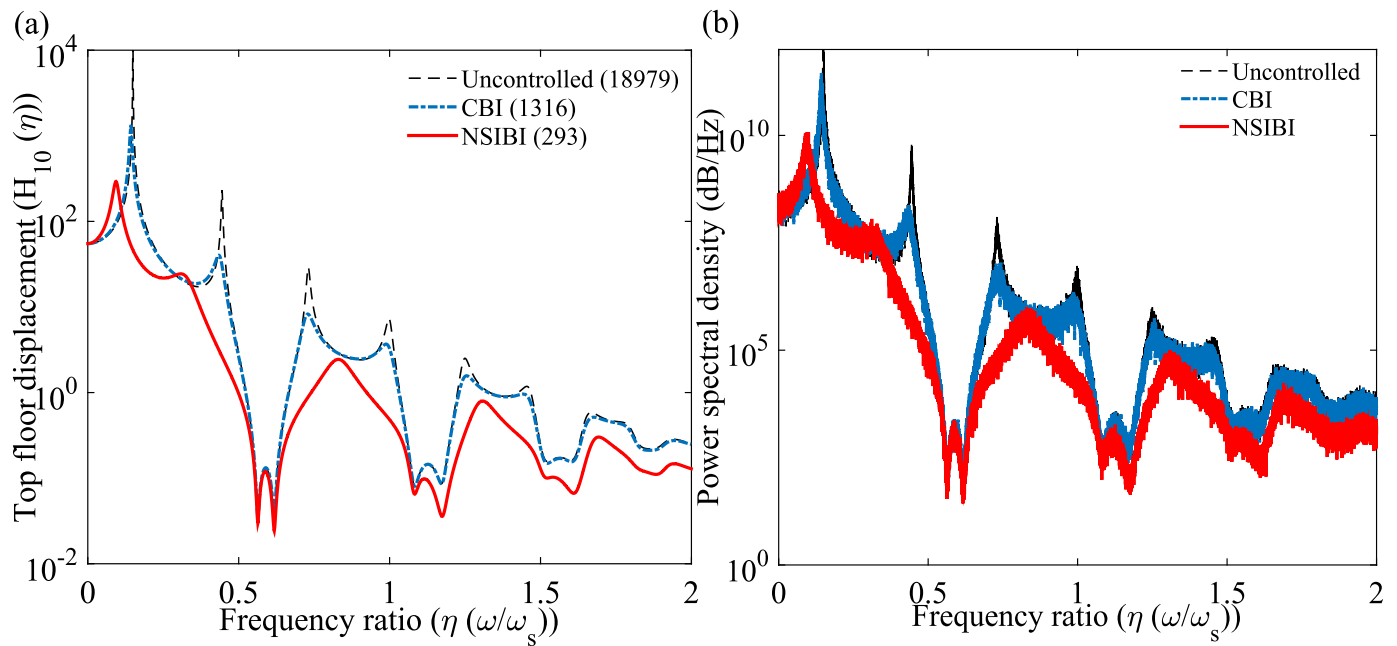


Fig. 20. The variations of optimal dynamic responses of top floor of ten storey building versus frequency ratio for different values of viscous damping ratio of NSIBI.

Table 7

The maximum acceleration of top floor of uncontrolled and isolated buildings and the acceleration response reduction capacity of NSIBI w.r.t CBI ( $A_{10}$  (%)) for ten-storey buildings.

Earthquake	$\ddot{x}_{10}^{max}$ ( $m/s^2$ )			$A_{10}$ (%)
	Uncontrolled	CBI	NSIBI	
Irpinia, Italy-01	0.401	0.3385	0.1058	68.74
Superstition Hills-02	0.7489	0.619	0.2658	57.06
Loma Prieta	0.5155	0.4493	0.1978	55.98
Erzican, Turkey	0.9006	0.8158	0.3607	55.79
Cape Mendocino	0.6457	0.4841	0.2505	48.25
Landers	0.9014	0.6268	0.3183	49.22
Northridge-01	1.4699	1.2898	0.4985	61.35
Kocaeli, Turkey	0.2354	0.1784	0.0881	50.62
Chi-Chi, Taiwan	0.7566	0.7162	0.3493	51.23
Chi-Chi, Taiwan	0.6902	0.5243	0.2399	54.24
Duzce, Turkey	0.6387	0.4867	0.188	61.37
Average	0.719	0.594	0.260	55.80

in Table 7. The mathematical formulation to determine the acceleration response reduction capacity of NSIBI w.r.t CBI ( $A_{10}$  (%)) for ten-storey buildings derives as

$$A_{10} (\%) = \frac{(\ddot{x}_{10}^{max})_{CBI} - (\ddot{x}_{10}^{max})_{NSIBI}}{(\ddot{x}_{10}^{max})_{CBI}} \quad (18)$$

The bar diagram of the normalized maximum displacement of the main structure’s top floor subjected to near-field earthquake base excitations has been shown in Fig. 23(a).

The bar plot for the optimum NSIBI-isolated structure’s displacement profile is comparatively less than the bar plot of the displacement profile of structures isolated by optimum CBI. Therefore, the displacement reduction capacity of the optimum NSIBI is significantly more than the optimum CBI. The bar diagram of the normalized maximum acceleration of the main structure’s top floor subjected to near-field earthquake base excitations has been shown in Fig. 23(b). The bar plot for the optimum NSIBI-isolated structure’s acceleration profile is comparatively less than the bar plot of the acceleration profile of structures isolated by optimum CBI. Therefore, the acceleration reduction capacity of the optimum NSIBI is significantly more than the optimum CBI. The variations of top floor damping forces of uncontrolled ten-storey buildings and buildings isolated by CBI and NSIBI have been

shown in Fig. 24. Fig. 24 indicates that the damping force reduction capacity of NSIBI is significantly superior to the CBI. The variations of kinetic, potential, and dissipated energy of the uncontrolled structure versus time subjected to Northridge-01 earthquake base excitation have been shown in Fig. 25, structure isolated by CBI, and structure isolated by NSIBI have been shown in Figs. 25(b) and 25(c). The energy profiles of the uncontrolled structure and structure isolated by CBI is much more than that of the structure isolated by NSIBI. The energy profile of both isolators has also been determined. Therefore, the variations of the kinetic, potential, and dissipated energy profile of the CBI subjected to Northridge-01 earthquake base excitation have been shown in Fig. 26(a) and the energy profile of the NSIBI has been shown in Fig. 26(b). The energy dissipation capacity of the NSIBI is significantly greater than the energy dissipation capacity of CBI.

### 6. Summary and conclusions

This paper introduces the optimum negative stiffness inerter-based vibration isolators to mitigate the dynamic responses of multi-storey buildings. The exact closed-form expression for optimal design parameters, such as frequency and viscous damping ratio of NSIBI installed in the multi-storey building, are derived employing the  $H_2$  optimization method. The frequency and time domain responses of the isolated structures are determined to assess the efficiency of the optimal design parameters as well as the dynamic response reduction capacity of optimum NSIBI w.r.t the optimum CBI. The significant results of the study are listed below.

- A higher base mass ratio, higher inerter mass ratio, and lower stiffness ratio are recommended to achieve a lower frequency ratio for optimum NSIBI.
- A higher base mass ratio, a higher inerter mass ratio, and a lower stiffness ratio are recommended to design the optimum NSIBI for achieving the optimal viscous damping ratio for NSIBI in the affordable range. As a result, the viscous damping ratio stood between 0.1 to 1.0, i.e.,  $0.1 \leq \zeta_b \leq 0.9$ , which is practically implementable and affordable.
- Initially, these novel isolators are applied to the five-storey buildings. According to the frequency domain analysis, the dynamic response reduction capacities of NSIBI are significantly 51.93% and

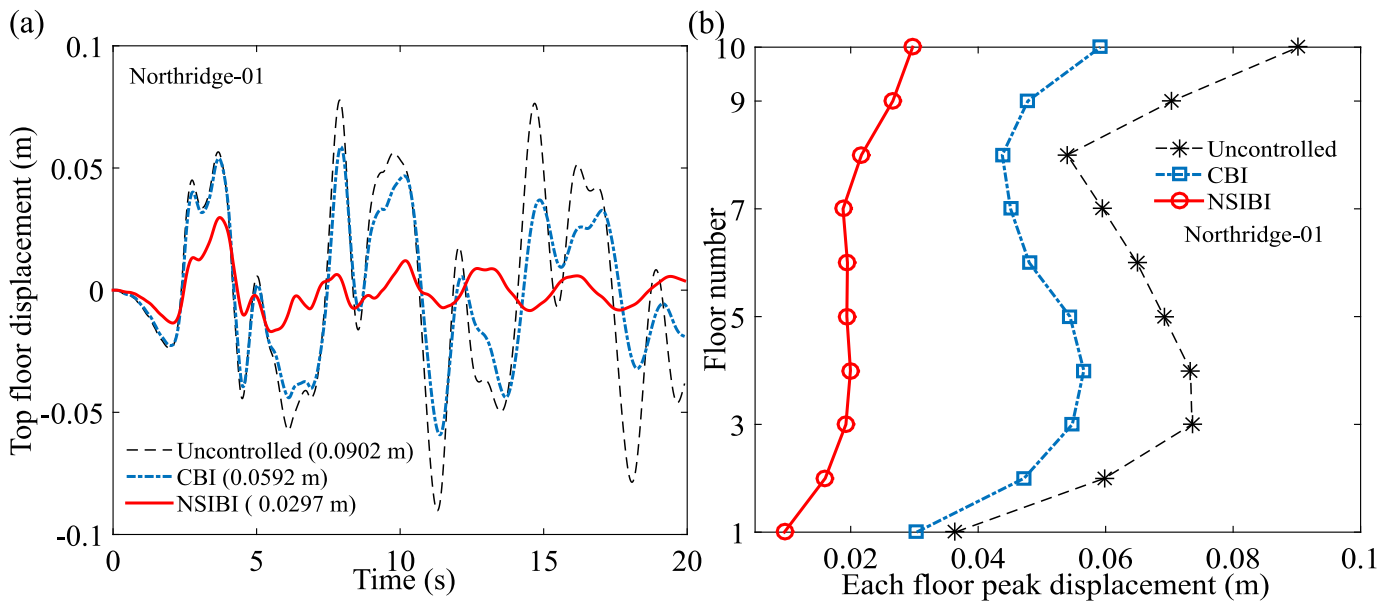


Fig. 21. The variations of optimal dynamic responses of top floor of ten storey building versus frequency ratio for different values of viscous damping ratio of NSIBI.

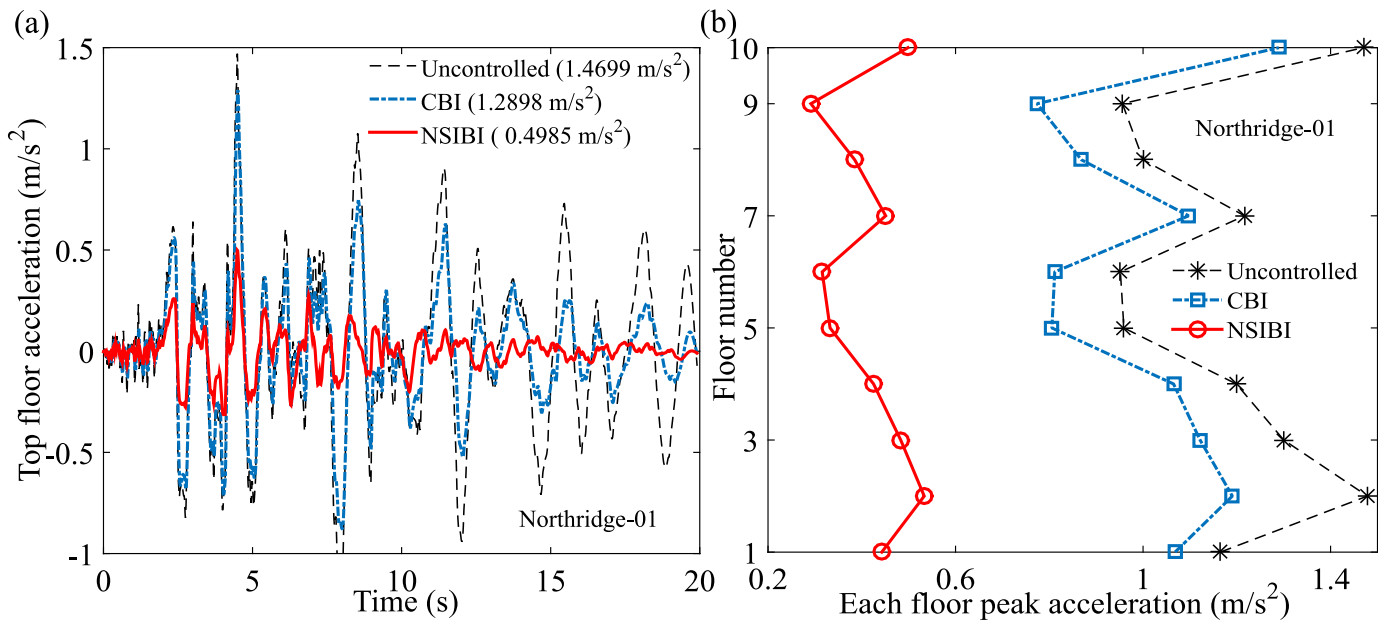


Fig. 22. The variations of optimal dynamic responses of top floor of ten storey building versus frequency ratio for different values of viscous damping ratio of NSIBI.

81.24% superior to the CBI when all the buildings are subjected to harmonic and random-white base excitations, respectively. According to the numerical study, the displacement and acceleration reduction capacities of NSIBI are significantly 57.59% and 55.39% superior to the CBI subjected to near-field earthquake base excitations (pulse records).

- Later, these novel isolators are applied to the ten-storey buildings. According to the frequency domain analysis, the dynamic response reduction capacities of NSIBI are significantly 77.73% and 94.02% superior to the CBI when all the buildings are subjected to harmonic and random-white base excitations, respectively. According to the numerical study, the displacement and acceleration reduction capacities of NSIBI are significantly 56.42% and 55.80% superior to the CBI subjected to near-field earthquake base excitations (pulse records).

- The vibration reduction capacity of optimum CBI is significantly decreasing while the storey level of the multi-storey buildings increases, whereas NSIBI is still efficient in reducing the dynamic responses effectively.

All the results of this study have been determined mathematically, i.e., analytically and numerically, in terms of closed-form expressions. All of the results are mathematically accurate. Therefore, the  $H_2$  optimized closed-form expressions for novel NSIBI, along with the solutions methods for dynamic response estimation, are applicable for practical implementation. The introduction of negative stiffness inerter-based base isolators, along with the exact closed-form expressions for optimal design parameters of NSIBI for multi-storey buildings, is one of the significant contributions of this paper. These closed-form expressions provide optimal design to NSIBI, increasing the novel isolator's vibration isolation capacity. These novel isolators are cost-effective and provide more vibration reduction capacity than conventional base

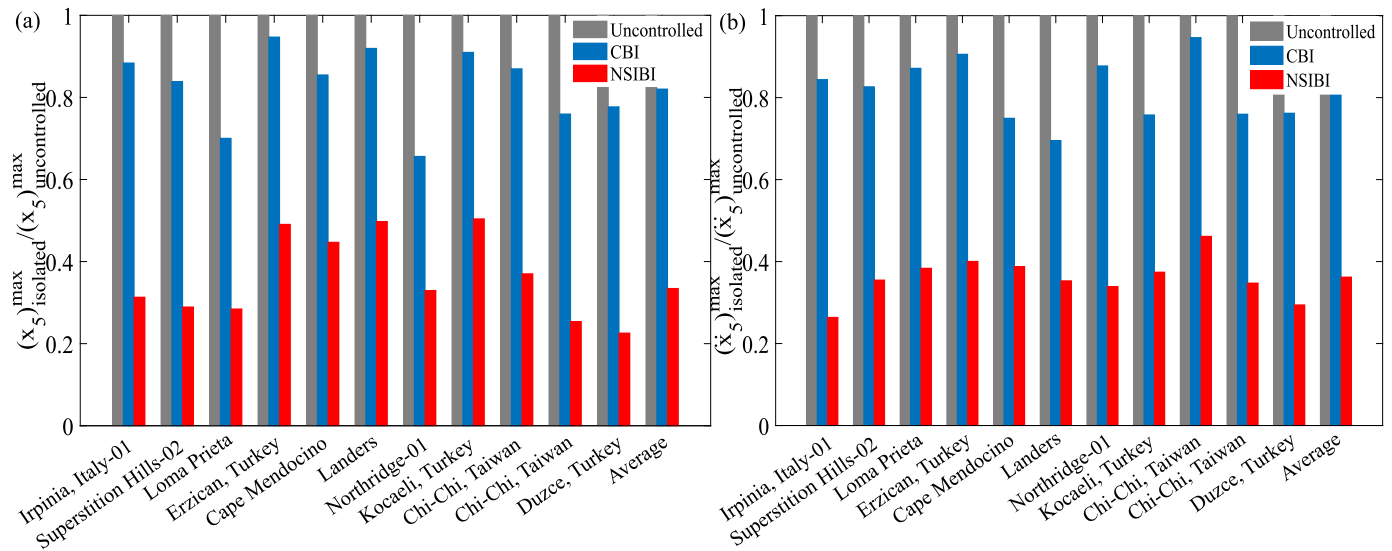


Fig. 23. The normalized (a) maximum displacement and (b) maximum acceleration of the main structure’s top floor subjected near-field earthquake base excitations.

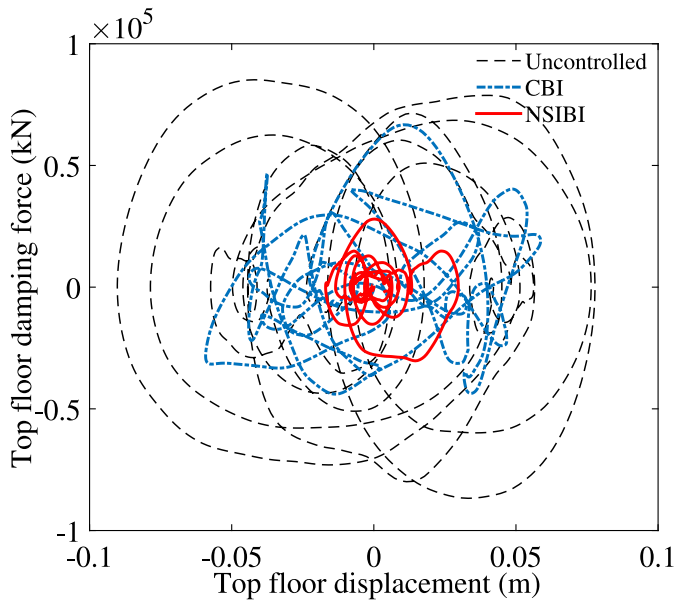


Fig. 24. The variations of top floor damping forces of uncontrolled ten-storey building and building isolated by CBI and NSIBI.

isolators without increasing the static mass. The experimentation and prototyping of the novel isolators for structures are the continuations of the present study, as suggested by the coauthors.

**Declaration of competing interest**

The authors declare that they have no known competing financial interests or personal relationships that could have appeared to influence the work reported in this paper.

**Acknowledgements**

The authors’ would like to acknowledge the Inspire faculty grant, grant number DST/INSPIRE/04/2018/000052 for partial financial support for the project. SC would like to acknowledge the MHRD grant received from IIT Delhi, India during the period of this research work.

**Appendix A. Closed-form expression for dynamic response**

The dynamic response of the NSIBI has been derived as

$$H_b(q) = \frac{X_b}{A_g} \frac{-q^{10}\mu_b - 9q^8\mu_b\omega_s^2 - 28q^6\mu_b\omega_s^4 - 35q^4\mu_b\omega_s^6 - 15q^2\mu_b\omega_s^8 - \omega_s^{10}\mu_b - \omega_s^2q^8 - 8\omega_s^4q^6 - 21\omega_s^6q^4 - 20\omega_s^8q^2 - 5\omega_s^{10}}{\Delta} \tag{A.1}$$

$\Delta$  has been derived as

$$\Delta = \begin{aligned} & (\mu_b + \mu_d)q^{12} + (2\zeta_b\mu_b\omega_b + 2\zeta_b\mu_d\omega_b)q^{11} \\ & + \left( -\beta\mu_b\omega_b^2 - \beta\mu_d\omega_b^2 + \mu_b\omega_b^2 + 9\omega_s^2\mu_b + \mu_d\omega_b^2 + 9\omega_s^2\mu_d + \omega_s^2 \right)q^{10} \\ & + (18\zeta_b\mu_b\omega_b\omega_s^2 + 18\zeta_b\mu_d\omega_b\omega_s^2)q^9 \\ & + \left( -9\beta\mu_b\omega_b^2\omega_s^2 - 9\beta\mu_d\omega_b^2\omega_s^2 + 9\mu_b\omega_b^2\omega_s^2 + 28\omega_s^4\mu_b + 9\mu_d\omega_b^2\omega_s^2 + 28\mu_d\omega_s^4 + 8\omega_s^4 \right)q^8 \\ & + (56\zeta_b\mu_b\omega_b\omega_s^4 + 56\zeta_b\mu_d\omega_b\omega_s^4)q^7 \\ & + \left( -28\beta\mu_b\omega_b^2\omega_s^4 - 28\beta\mu_d\omega_b^2\omega_s^4 + 28\mu_b\omega_b^2\omega_s^4 + 35\omega_s^6\mu_b + 28\mu_d\omega_b^2\omega_s^4 + 35\mu_d\omega_s^6 + 21\omega_s^6 \right)q^6 \\ & + (70\zeta_b\mu_b\omega_b\omega_s^6 + 70\zeta_b\mu_d\omega_b\omega_s^6)q^5 \\ & + \left( -35\beta\mu_b\omega_b^2\omega_s^6 - 35\beta\mu_d\omega_b^2\omega_s^6 + 35\mu_b\omega_b^2\omega_s^6 + 15\omega_s^8\mu_b + 35\mu_d\omega_b^2\omega_s^6 + 15\mu_d\omega_s^8 + 20\omega_s^8 \right)q^4 \\ & + (30\zeta_b\mu_b\omega_b\omega_s^8 + 30\zeta_b\mu_d\omega_b\omega_s^8)q^3 \\ & + \left( -15\beta\mu_b\omega_b^2\omega_s^8 - 15\beta\mu_d\omega_b^2\omega_s^8 + 15\mu_b\omega_b^2\omega_s^8 + \omega_s^{10}\mu_b + 15\mu_d\omega_b^2\omega_s^8 + \mu_d\omega_s^{10} + 5\omega_s^{10} \right)q^2 \\ & + (2\zeta_b\mu_b\omega_b\omega_s^{10} + 2\zeta_b\mu_d\omega_b\omega_s^{10})q \\ & - \beta\mu_b\omega_b^2\omega_s^{10} - \beta\mu_d\omega_b^2\omega_s^{10} + \mu_b\omega_b^2\omega_s^{10} + \mu_d\omega_b^2\omega_s^{10} \end{aligned} \tag{A.2}$$

**Appendix B. The mathematical formulation to determine the standard deviation of dynamic responses**

$$\int_{-\infty}^{\infty} \frac{\varepsilon_n(\omega) d\omega}{Y_n(i\omega)Y_n^*(i\omega)} = \frac{\pi}{r_{12}} \frac{\det[\mathbf{N}_{12}]}{\det[\mathbf{D}_{12}]} \tag{B.1}$$

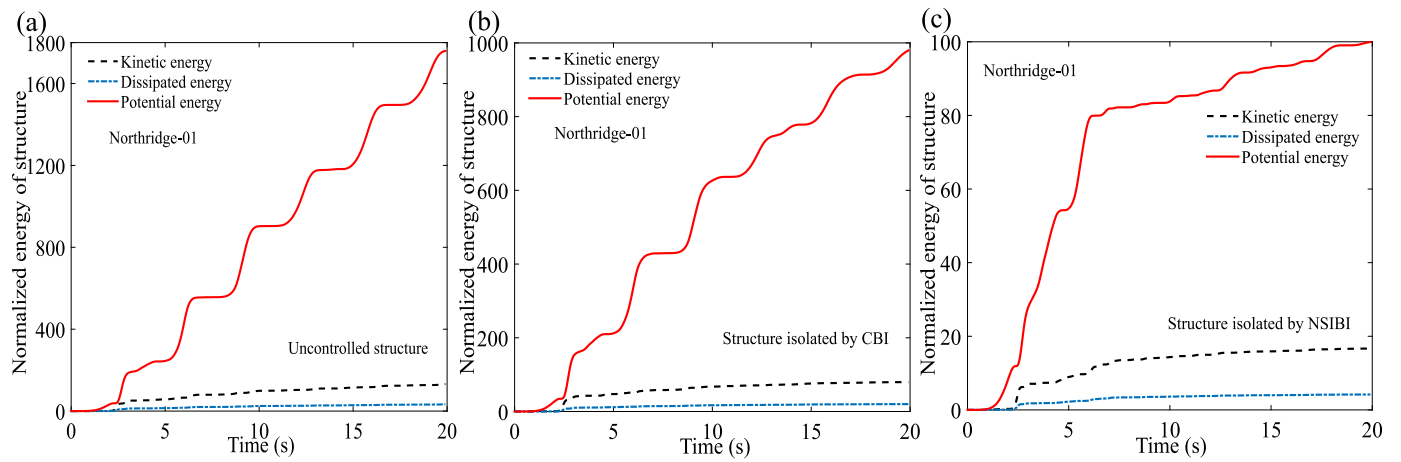


Fig. 25. The variations of kinetic, potential, and dissipated energy of the (a) uncontrolled structure, (b) structure isolated by CBI, and (c) structure isolated by NSIBI versus time subjected to Northridge-01 earthquake base excitation.

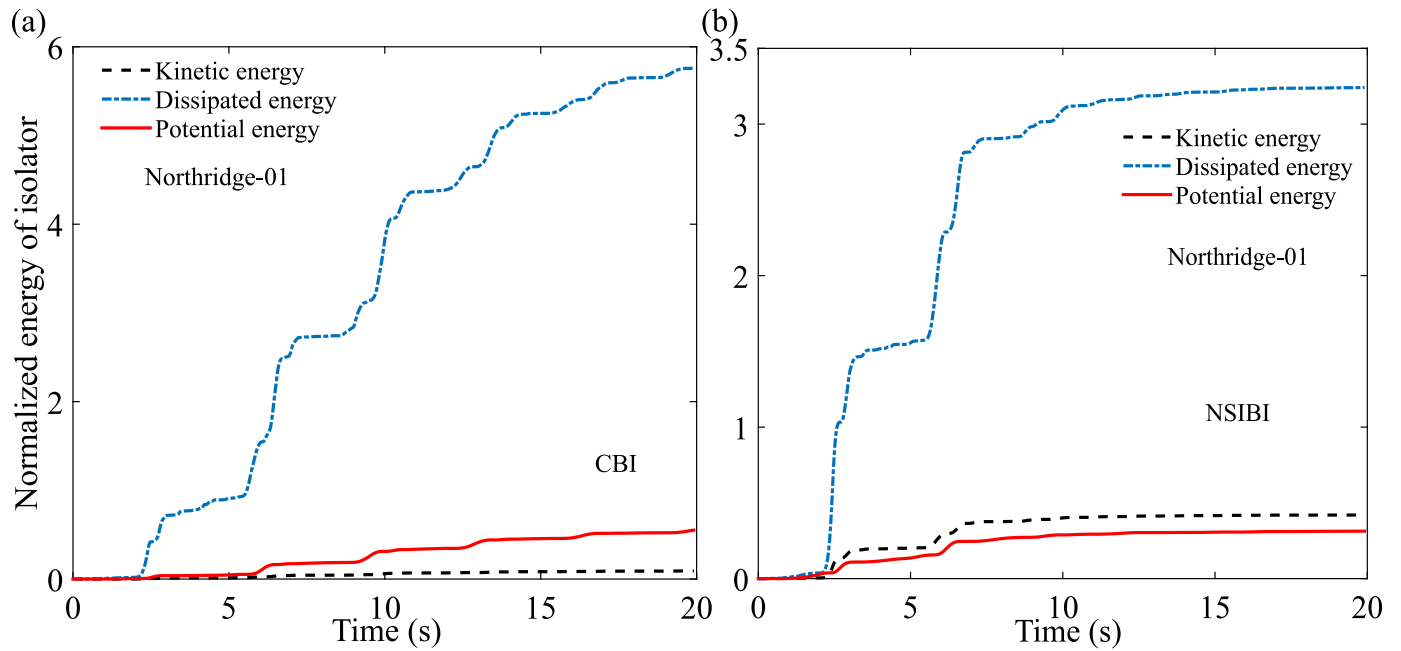


Fig. 26. The variations of kinetic, potential, and dissipated energy of the (a) CBI and (b) NSIBI versus time subjected to Northridge-01 earthquake base excitation.

$$N_n = \begin{bmatrix} h_{11} & h_{10} & h_9 & h_8 & h_7 & h_6 & h_5 & h_4 & h_3 & h_2 & h_1 & h_0 \\ -r_{12} & r_{10} & -r_8 & r_6 & -r_4 & r_2 & -r_0 & 0 & 0 & 0 & 0 & 0 \\ 0 & -r_{11} & r_9 & -r_7 & r_5 & -r_3 & r_1 & 0 & 0 & 0 & 0 & 0 \\ 0 & r_{12} & -r_{10} & r_8 & -r_6 & r_4 & -r_2 & r_0 & 0 & 0 & 0 & 0 \\ 0 & 0 & r_{11} & -r_9 & r_7 & -r_5 & r_3 & -r_1 & 0 & 0 & 0 & 0 \\ 0 & 0 & -r_{12} & r_{10} & -r_8 & r_6 & -r_4 & r_2 & -r_0 & 0 & 0 & 0 \\ 0 & 0 & 0 & -r_{11} & r_9 & -r_7 & r_5 & -r_3 & r_1 & 0 & 0 & 0 \\ 0 & 0 & 0 & r_{12} & -r_{10} & r_8 & -r_6 & r_4 & -r_2 & r_0 & 0 & 0 \\ 0 & 0 & 0 & 0 & r_{11} & -r_9 & r_7 & -r_5 & r_3 & -r_1 & 0 & 0 \\ 0 & 0 & 0 & 0 & r_{12} & -r_{10} & r_8 & -r_6 & r_4 & -r_2 & r_0 & 0 \\ 0 & 0 & 0 & 0 & 0 & r_{11} & -r_9 & r_7 & -r_5 & r_3 & -r_1 & 0 \\ 0 & 0 & 0 & 0 & 0 & -r_{12} & r_{10} & -r_8 & r_6 & -r_4 & r_2 & -r_0 \\ 0 & 0 & 0 & 0 & 0 & 0 & -r_{11} & r_9 & -r_7 & r_5 & -r_3 & r_1 \\ 0 & 0 & 0 & 0 & 0 & 0 & r_{12} & -r_{10} & r_8 & -r_6 & r_4 & -r_2 & r_0 \end{bmatrix} \quad (B.2)$$

$$D_n = \begin{bmatrix} r_{11} & -r_9 & r_7 & -r_5 & r_3 & -r_1 & 0 & 0 & 0 & 0 & 0 & 0 \\ -r_{12} & r_{10} & -r_8 & r_6 & -r_4 & r_2 & -r_0 & 0 & 0 & 0 & 0 & 0 \\ 0 & -r_{11} & r_9 & -r_7 & r_5 & -r_3 & r_1 & 0 & 0 & 0 & 0 & 0 \\ 0 & r_{12} & -r_{10} & r_8 & -r_6 & r_4 & -r_2 & r_0 & 0 & 0 & 0 & 0 \\ 0 & 0 & r_{11} & -r_9 & r_7 & -r_5 & r_3 & -r_1 & 0 & 0 & 0 & 0 \\ 0 & 0 & -r_{12} & r_{10} & -r_8 & r_6 & -r_4 & r_2 & -r_0 & 0 & 0 & 0 \\ 0 & 0 & 0 & -r_{11} & r_9 & -r_7 & r_5 & -r_3 & r_1 & 0 & 0 & 0 \\ 0 & 0 & 0 & r_{12} & -r_{10} & r_8 & -r_6 & r_4 & -r_2 & r_0 & 0 & 0 \\ 0 & 0 & 0 & 0 & r_{11} & -r_9 & r_7 & -r_5 & r_3 & -r_1 & 0 & 0 \\ 0 & 0 & 0 & 0 & -r_{12} & r_{10} & -r_8 & r_6 & -r_4 & r_2 & -r_0 & 0 \\ 0 & 0 & 0 & 0 & 0 & -r_{11} & r_9 & -r_7 & r_5 & -r_3 & r_1 & 0 \\ 0 & 0 & 0 & 0 & 0 & 0 & -r_{12} & r_{10} & -r_8 & r_6 & -r_4 & r_2 & -r_0 \\ 0 & 0 & 0 & 0 & 0 & 0 & 0 & -r_{11} & r_9 & -r_7 & r_5 & -r_3 & r_1 \\ 0 & 0 & 0 & 0 & 0 & 0 & 0 & r_{12} & -r_{10} & r_8 & -r_6 & r_4 & -r_2 & r_0 \end{bmatrix} \quad (B.3)$$

Hence, the modified SD has been listed in Appendix B

$$\sigma_{x_s}^2 = \frac{S_0 2\pi \sqrt{55} \left( \begin{array}{l} 671\beta^2\mu_b^2\omega_b^4 + 1342\beta^2\mu_b\mu_d\omega_b^4 + 671\beta^2\mu_d^2\omega_b^4 \\ -1342\beta\mu_b^2\omega_b^4 - 2684\beta\mu_b\mu_d\omega_b^4 + 110\beta\mu_b\mu_d\omega_b^2\omega_s^2 \\ -1342\beta\mu_d^2\omega_b^4 + 110\beta\mu_d^2\omega_b^2\omega_s^2 - 225\beta\mu_b\omega_b^2\omega_s^2 \\ -225\beta\mu_d\omega_b^2\omega_s^2 + 671\mu_b^2\omega_b^4 + 1342\mu_b\mu_d\omega_b^4 \\ -110\mu_b\mu_d\omega_b^2\omega_s^2 + 671\mu_d^2\omega_b^4 - 110\mu_d^2\omega_b^2\omega_s^2 \\ + 5\mu_d^2\omega_s^4 + 225\mu_b\omega_b^2\omega_s^2 + 225\mu_d\omega_b^2\omega_s^2 \end{array} \right)}{\omega_b^2\omega_s^2(\mu_b + \mu_d)^2} \quad (B.4)$$

References

[1] Li Z, Huang G, Chen X, Zhou X. Seismic response and parametric analysis of inter-story isolated tall buildings based on enhanced simplified dynamic model. *Int J Struct Stab Dyn* 2022;22(03n04):2240008.

[2] Zhang S, Hu Y, Liu X, Tan P, Guo X. Hybrid isolation strategy for seismically isolated multi-tower building with a large podium. *Int J Struct Stab Dyn* 2022;2250061.

[3] Konar T, Ghosh AD. Adaptation of a deep liquid-containing tank into an effective structural vibration control device by a submerged cylindrical pendulum appendage. *Int J Struct Stab Dyn* 2021;21(06):2150078.

[4] Han H, Sorokin V, Tang L, Cao D. Lightweight origami isolators with deployable mechanism and quasi-zero-stiffness property. *Aerosp Sci Technol* 2022;107319.

[5] Liu F, Yu D, Wang C, Wang G. Advances in variable stiffness vibration isolator and its application in spacecraft. *Int J Struct Stab Dyn* 2022;2230004.

[6] Furinghetti M, Yang T, Calvi PM, Pavese A. Experimental evaluation of extra-stroke displacement capacity for Curved Surface Slider devices. *Soil Dyn Earth Eng* 2021;146:106752.

[7] Sheng T, Liu G-b, Bian X-c, Shi W-x, Chen Y. Development of a three-directional vibration isolator for buildings subject to metro-and earthquake-induced vibrations. *Eng Struct* 2022;252:113576.

[8] Shrimali M, Jangid R. A comparative study of performance of various isolation systems for liquid storage tanks. *Int J Struct Stab Dyn* 2002;2(04):573–91.

[9] Bai X-X, Jiang P, Qian L-J. Integrated semi-active seat suspension for both longitudinal and vertical vibration isolation. *J Intell Mater Syst Struct* 2017;28(8):1036–49.

[10] Chen MC, Restrepo JI, Blandon C, Velásquez JF. Performance-based seismic design framework for inertia-sensitive nonstructural components in base-isolated buildings. *J Build Eng* 2021;43:103073.

[11] Losanno D, Ravichandran N, Parisi F. Seismic fragility of base-isolated single-storey unreinforced masonry buildings equipped with classical and recycled rubber bearings in Himalayan regions. *J Build Eng* 2022;45:103648.

[12] Chowdhury S, Banerjee A. The exact closed-form equations for optimal design parameters of enhanced inerter-based isolation systems. *J Vib Control* 2022;10775463221133428.

[13] Nagarajaiah S, Narasimhan S. Smart base-isolated benchmark building. Part II: phase I sample controllers for linear isolation systems. *Struct Control Health Monit* 2006;13(2–3):589–604, The Official Journal of the International Association for Structural Control and Monitoring and of the European Association for the Control of Structures.

[14] Inaudi JA, Kelly JM. Optimum damping in linear isolation systems. *Earthq Eng Struct Dyn* 1993;22(7):583–98.

[15] Kelly JM. The role of damping in seismic isolation. *Earthq Eng Struct Dyn* 1999;28(1):3–20.

[16] Chowdhury S, Banerjee A, Adhikari S. The optimal design of dynamic systems with negative stiffness inertial amplifier tuned mass dampers. *Appl Math Model* 2023;114:694–721.

[17] Chowdhury S, Banerjee A, Adhikari S. The optimum inertial amplifier tuned mass dampers for nonlinear dynamic systems. *Int J Appl Mech (ja)*. <http://dx.doi.org/10.1142/S1758825123500096>.

[18] Adhikari S, Woodhouse J. Identification of damping: part 1, viscous damping. *J Sound Vib* 2001;243(1):43–61.

[19] Kikuchi M, Aiken ID. An analytical hysteresis model for elastomeric seismic isolation bearings. *Earthq Eng Struct Dyn* 1997;26(2):215–31.

[20] Buckle IG. New Zealand seismic base isolation concepts and their application to nuclear engineering. *Nucl Eng Des* 1985;84(3):313–26.

[21] Robinson WH. Lead-rubber hysteretic bearings suitable for protecting structures during earthquakes. *Earthq Eng Struct Dyn* 1982;10(4):593–604.

[22] Jangid R. Computational numerical models for seismic response of structures isolated by sliding systems. *Struct Control Health Monit* 2005;12(1):117–37.

[23] Jangid R. Optimum friction pendulum system for near-fault motions. *Eng Struct* 2005;27(3):349–59.

[24] Zhang J, Ding Y, Guan X. Overturning resistance of friction pendulum bearing-isolated structure subjected to impact. *Int J Struct Stab Dyn* 2022;22(06):2250072.

[25] Shakib H, Fuladgar A. Response of pure-friction sliding structures to three components of earthquake excitation. *Comput Struct* 2003;81(4):189–96.

[26] Mostaghel N, Khodaverdian M. Dynamics of resilient-friction base isolator (R-FBI). *Earthq Eng Struct Dyn* 1987;15(3):379–90.

[27] Kalpakidis IV, Constantinou MC, Whittaker AS. Modeling strength degradation in lead-rubber bearings under earthquake shaking. *Earthq Eng Struct Dyn* 2010;39(13):1533–49.

[28] Quagliani V, Dubini P, Furinghetti M, Pavese A. Assessment of scale effects in the experimental evaluation of the coefficient of friction of sliding isolators. *J Earthq Eng* 2022;26(1):525–45.

[29] Kumar M, Whittaker AS, Constantinou MC. An advanced numerical model of elastomeric seismic isolation bearings. *Earthq Eng Struct Dyn* 2014;43(13):1955–74.

[30] Kumar M, Whittaker AS. Cross-platform implementation, verification and validation of advanced mathematical models of elastomeric seismic isolation bearings. *Eng Struct* 2018;175:926–43.

[31] Cardone D, Viggiani L, Perrone G, Telesca A, Di Cesare A, Pozzo F, et al. Modelling and seismic response analysis of existing Italian residential RC buildings retrofitted by seismic isolation. *J Earthq Eng* 2022;1–25.

[32] Kumar M, Whittaker AS, Constantinou MC. Experimental investigation of cavitation in elastomeric seismic isolation bearings. *Eng Struct* 2015;101:290–305.

[33] Chowdhury S, Banerjee A, Adhikari S. Optimal design of inertial amplifier base isolators for dynamic response control of multi-storey buildings. *Int J Struct Stab Dyn* 2022;2350047.

[34] Chowdhury S, Banerjee A. The exact closed-form expressions for optimal design parameters of resonating base isolators. *Int J Mech Sci* 2022;224:107284.

[35] Cheng Z, Palermo A, Shi Z, Marzani A. Enhanced tuned mass damper using an inertial amplification mechanism. *J Sound Vib* 2020;115267.

[36] Patro SR, Banerjee A, Adhikari S, Ramana G. Kaimal spectrum based H2 optimization of tuned mass dampers for wind turbines. *J Vib Control* 2022;10775463221092838.

[37] Baduidana M, Kenfack-Jiotsa A. Optimal design of inerter-based isolators minimizing the compliance and mobility transfer function versus harmonic and random ground acceleration excitation. *J Vib Control* 2021;27(11–12):1297–310.

[38] Čakmak D, Tomičević Z, Wolf H, Božić Ž, Semenski D. Stability and performance of supercritical inerter-based active vibration isolation systems. *J Sound Vib* 2021;116234.

[39] Hu Y, Chen MZ. Performance evaluation for inerter-based dynamic vibration absorbers. *Int J Mech Sci* 2015;99:297–307.

[40] Chowdhury S, Banerjee A, Adhikari S. Optimal negative stiffness inertial-amplifier-base-isolators: Exact closed-form expressions. *Int J Mech Sci* 2022;107044.

[41] Hu Y, Chen MZ, Shu Z, Huang L. Analysis and optimisation for inerter-based isolators via fixed-point theory and algebraic solution. *J Sound Vib* 2015;346:17–36.

[42] Qian F, Luo Y, Sun H, Tai WC, Zuo L. Optimal tuned inerter dampers for performance enhancement of vibration isolation. *Eng Struct* 2019;198:109464.

[43] Adhikari S, Banerjee A. Enhanced low-frequency vibration energy harvesting with inertial amplifiers. *J Intell Mater Syst Struct* 2021;1045389X211032281.

[44] Chowdhury S, Banerjee A. The exact closed-form expressions for optimal design parameters of resonating base isolators. *Int J Mech Sci* 2022;224:107284.

[45] Wilde K, Gardoni P, Fujino Y. Base isolation system with shape memory alloy device for elevated highway bridges. *Eng Struct* 2000;22(3):222–9.

[46] Anajafi H, Medina RA. Comparison of the seismic performance of a partial mass isolation technique with conventional TMD and base-isolation systems under broad-band and narrow-band excitations. *Eng Struct* 2018;158:110–23.

[47] De Domenico D, Ricciardi G. An enhanced base isolation system equipped with optimal tuned mass damper inerter (TMDI). *Earthq Eng Struct Dyn* 2018;47(5):1169–92.

[48] Smith MC. Synthesis of mechanical networks: the inerter. *IEEE Trans Automat Control* 2002;47(10):1648–62.

[49] Smith MC, Wang F-C. Performance benefits in passive vehicle suspensions employing inerters. *Veh Syst Dyn* 2004;42(4):235–57.

[50] Wang F-C, Liao M-K, Liao B-H, Su W-J, Chan H-A. The performance improvements of train suspension systems with mechanical networks employing inerters. *Veh Syst Dyn* 2009;47(7):805–30.

[51] Chowdhury S, Banerjee A, Adhikari S. Enhanced seismic base isolation using inertial amplifiers. *Structures* 2021;33:1340–53. <http://dx.doi.org/10.1016/j.istruc.2021.04.089>, URL <https://www.sciencedirect.com/science/article/pii/S23520124211003908>.

- [52] Banerjee A, Adhikari S, Hussein MI. Inertial amplification band-gap generation by coupling a levered mass with a locally resonant mass. *Int J Mech Sci* 2021;106630.
- [53] Bhatt A, Banerjee A. Double attenuation peaks in metamaterial with simultaneous negative mass and stiffness. *Phys Lett A* 2022;128201.
- [54] Hussein MI, Patrick I, Banerjee A, Adhikari S. Metadamping in inertially amplified metamaterials: Trade-off between spatial attenuation and temporal attenuation. *J Sound Vib* 2022;531:116977.
- [55] Yilmaz C, Hulbert GM, Kikuchi N. Phononic band gaps induced by inertial amplification in periodic media. *Phys Rev B* 2007;76(5):054309.
- [56] Xiang S, Songye Z. A comparative study of vibration isolation performance using negative stiffness and inerter dampers. *J Franklin Inst B* 2019;356(14):7922–46.
- [57] Zhao Z, Chen Q, Hu X, Zhang R. Enhanced energy dissipation benefit of negative stiffness amplifying dampers. *Int J Mech Sci* 2022;107934.
- [58] Lu Z, Yu X, Lau S-K, Khoo BC, Cui F. Membrane-type acoustic metamaterial with eccentric masses for broadband sound isolation. *Appl Acoust* 2020;157:107003.
- [59] Graciá-Salgado R, García-Chocano VM, Torrent D, Sánchez-Dehesa J. Negative mass density and  $\rho$ -near-zero quasi-two-dimensional metamaterials: Design and applications. *Phys Rev B* 2013;88(22):224305.
- [60] Lončar J, Igrec B, Babić D. Negative-inertia converters: Devices manifesting negative mass and negative moment of inertia. *Symmetry* 2022;14(3):529.
- [61] Lu Z-X, Li X, Yang Z-Y, Xie F. Novel structure with negative Poisson's ratio and enhanced Young's modulus. *Compos Struct* 2016;138:243–52.
- [62] Shen L, Wang Z, Wang X, Wei K. Negative Poisson's ratio and effective Young's modulus of a vertex-based hierarchical re-entrant honeycomb structure. *Int J Mech Sci* 2021;206:106611.
- [63] Labora DC, Lopes AM, Machado JT. Time-fractional dependence of the shear force in some beam type problems with negative Young modulus. *Appl Math Model* 2020;80:668–82.
- [64] Xu N, Liu H-T, An M-R, Wang L. Novel 2D star-shaped honeycombs with enhanced effective Young's modulus and negative Poisson's ratio. *Extreme Mech Lett* 2021;43:101164.
- [65] Huang H, Sun C. Theoretical investigation of the behavior of an acoustic metamaterial with extreme Young's modulus. *J Mech Phys Solids* 2011;59(10):2070–81.
- [66] Lin F, Xiang Y, Shen H-S. Tunable positive/negative Young's modulus in graphene-based metamaterials. *Adv Theory Simul* 2021;4(2):2000130.
- [67] Shi X, Zhu S. Simulation and optimization of magnetic negative stiffness dampers. *Sensors Actuators A* 2017;259:14–33.
- [68] Wang M, Sun F-f, Jin H-j. Performance evaluation of existing isolated buildings with supplemental passive pseudo-negative stiffness devices. *Eng Struct* 2018;177:30–46.
- [69] Zhao F, Ji J, Ye K, Luo Q. An innovative quasi-zero stiffness isolator with three pairs of oblique springs. *Int J Mech Sci* 2021;192:106093.
- [70] Cheng C, Li S, Wang Y, Jiang X. On the analysis of a high-static-low-dynamic stiffness vibration isolator with time-delayed cubic displacement feedback. *J Sound Vib* 2016;378:76–91.
- [71] Fulcher BA, Shahan DW, Haberman MR, Conner Seepersad C, Wilson PS. Analytical and experimental investigation of buckled beams as negative stiffness elements for passive vibration and shock isolation systems. *J Vib Acoust* 2014;136(3).
- [72] Yuan S, Sun Y, Wang M, Ding J, Zhao J, Huang Y, et al. Tunable negative stiffness spring using maxwell normal stress. *Int J Mech Sci* 2021;193:106127.
- [73] Lakes RS, Lee T, Bersie A, Wang Y-C. Extreme damping in composite materials with negative-stiffness inclusions. *Nature* 2001;410(6828):565–7.
- [74] Roberts JB, Spanos PD. Random vibration and statistical linearization. Courier Corporation; 2003.